Molecular Diversity (2025) 29:6379–6400
https://doi.org/10.1007/s11030-025-11127-4

ORIGINAL ARTICLE

An innovative approach to development of new pyrazolylquinolin-2-one hybrids as dual EGFR and BRAF^{V600E} inhibitors

Mohamed M. Hawwas[1] · Ahmed S. Mancy[2,3] · Mohamed Ramadan[1] · Tarek S. Ibrahim[4,5] · Ashraf H. Bayoumi[6] · Mohamed Alswah[6]

Received: 28 December 2024 / Accepted: 3 February 2025 / Published online: 8 March 2025
© The Author(s) 2025

Abstract

Novel quinoline-based derivatives **2a–e** and **4a–j** have been designed and synthesized as potential antiproliferative agents. The designed compounds were screened for their antiproliferative activity against sixty cell lines according to NCI protocol. The promising hybrids **4d**–**g** are screened by MTT assays on three cancer cell lines: leukemia (MOLT-4), lung cancer (HOP-92), and breast cancer (T47D), with IC_{50} values ranging from 4.982 ± 0.2 to 36.52 ± 1.46 µM compared to Staurosporine, with compound **4e** being the most effective. Derivatives **4d–g** were evaluated for their inhibitory activity on EGFR and BRAF^{V600E}. Compound **4e** exhibited the highest inhibitory activities, with IC_{50} values of 0.055 ± 0.002 µM for EGFR and 0.068 ± 0.003 µM for BRAF^{V600E}, compared to the reference drugs erlotinib (IC_{50} 0.06 ± 0.002 µM) and vemurafenib (IC_{50} 0.035 ± 0.001 µM), respectively. Cell cycle analysis of the HOP-92 manifested that pre-G1 apoptosis signaling took place after **4e** treatment. Docking simulations were employed to analyze the modes and scores of compounds **4d–g** with respect to EGFR and BRAF^{V600E}. The results revealed that compound **4e** exhibited strong affinity for both EGFR and BRAF^{V600E} compared to the reference drugs with values of -3.226 and -3.474 kcal/mol, respectively.

Keywords Quinoline · Pyrazole · Antiproliferative · EGFR · BRAF^{V600E}

Introduction

Based on the revised projections from the International Agency for Research on Cancer (IARC), which breaks out worldwide cancer statistics by globe region for 2022, there were about 20 million new cases of cancer and 9.7 million cancer-related deaths [1]. Unfortunately, according to statistics, one in five men and women will have cancer at some point in their lives [2]. Biochemically, protein kinases are a family of enzymes that control a range of cellular biological processes, including apoptosis, proliferation, migration, metabolism, and finally normal cell growth and division [3]. Protein kinases regulate the previous biological process through interaction with its cell membrane-localized receptors, such as EGFR, VEGFR, c-Met, etc. [4]. Growth factors activate the EGFR, triggering a cascade of downstream waves within the cell that activate the RAS/RAF/MEK pathway. Consequently, the parallel pathways of PI3K/AKT/mTOR are stimulated by the activated intracellular RAS (Fig. 1) [5]. Overexpression, mutation, or disintegration of this tangled process results in uncontrolled cell division and proliferation [6]. Regarding cancer treatment

✉ Mohamed Ramadan
elbashamohammed@azhar.edu.eg

[1] Department of Pharmaceutical Organic Chemistry, Faculty of Pharmacy, Al-Azhar University, Assiut, Egypt

[2] Department of Pharmacology and Experimental Neuroscience, University of Nebraska Medical Center, Omaha, NE 68198, USA

[3] Department of Pharmaceutical Sciences, College of Pharmacy, University of Nebraska Medical Center, Omaha, Nebraska, USA

[4] Department of Pharmaceutical Chemistry, Faculty of Pharmacy, King Abdulaziz University, Jeddah 21589, Saudi Arabia

[5] Department of Pharmaceutical Organic Chemistry, Faculty of Pharmacy, Zagazig University, Zagazig 44519, Egypt

[6] Department of Pharmaceutical Organic Chemistry, Faculty of Pharmacy, Al-Azhar University, Cairo, Egypt

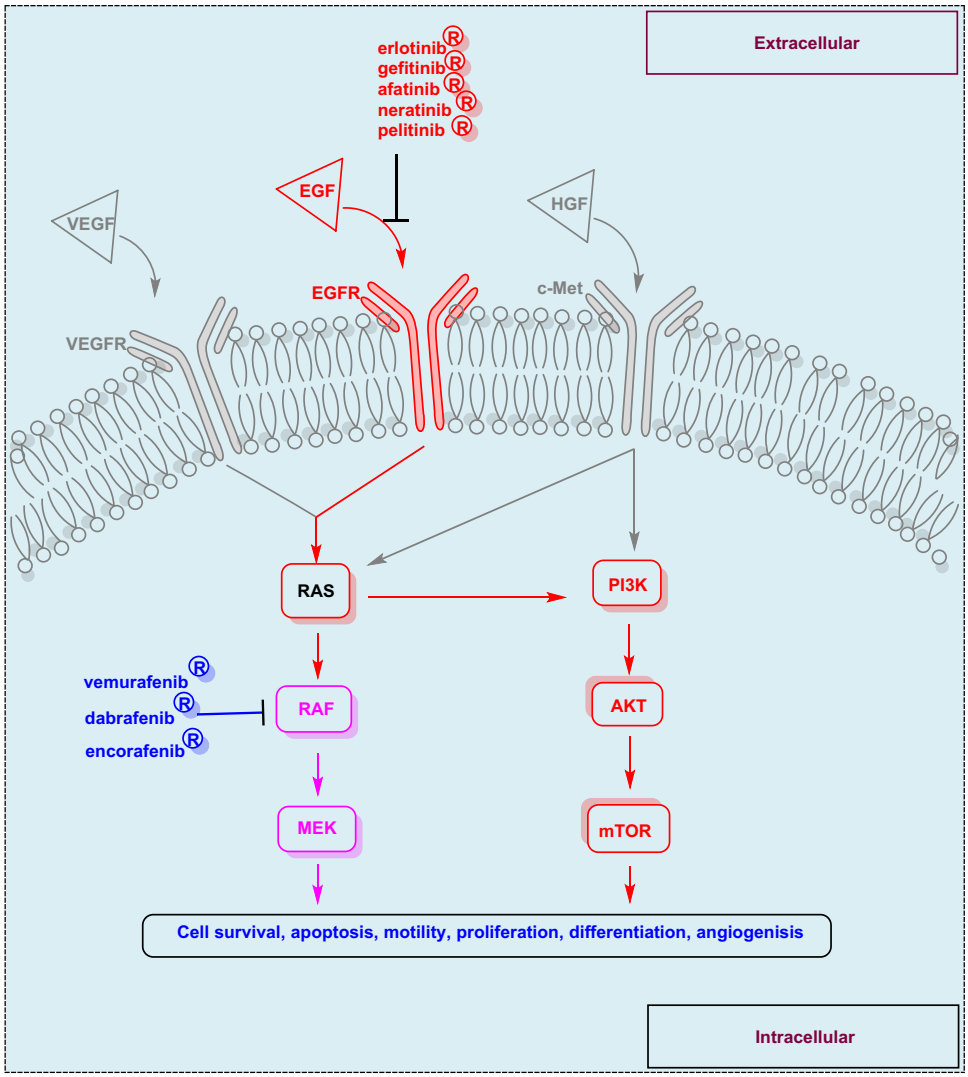


Fig. 1 Cell regulation due to EGFR, VEGFR, and c-Met downstream signals through RAS/RAF/MEK pathways

strategy, blocking EGFR leads to RAS/RAF/MEK and PI3K/AKT/mTOR signaling cascade suppression [7]. In addition, $BRAF^{V600E}$ is a significant intracellular protein that has recently been extensively studied as a distinct oncogenic element [8]. Unfavorable mutations in the $BRAF^{V600E}$ gene accelerate tumor growth, leading to uncontrolled cell proliferation [7]. The known $BRAF^{V600E}$ mutation was anticipated to serve as a resistance mechanism to much chemotherapy [9]. The development of resistance in cancer has also been linked to the feedback stimulation of EGFR signaling [10]. Hence, EGFR/BRAF (cetuximab/vemurafenib) was used to alleviate these issues according to studies on metastatic cases with $BRAF^{V600E}$ mutations [11]. Therefore, the EGFR activation problem might be resolved by sequentially inhibiting the two kinases. One tactic for coincident blocking of more than one target is combined chemotherapy [12]. Unfortunately, dangerous drug interactions and toxicity can occur while taking several drugs concomitantly [13]. Therefore, combining two medications into a single molecule that hits several targets may help with these problems [14]. Based on the above-mentioned importance of EGFR and $BRAF^{V600E}$ in controlling cell division and proliferation, dual targeting of EGFR and $BRAF^{V600E}$ kinases revealed a successful strategy to control cancers [15]. The low efficacy, resistance, or toxicity related to many single-target or combination-based medicines were overcome by these dual mechanistic medications [16], which also had a more acceptable posology. Subsequently, investigating this dual mechanism could result in a treatment that works well and has fewer adverse effects.

In this context, pyrazole derivatives (Lazertinib) **1** [17] (Mavelertinib) **2** [18] acted on EGFR as a single target (Fig. 2i-a); other pyrazole derivatives **3** (Encotafenib) [19] (GDC-9879) **4** [20] have the potential to inhibit $BRAF^{V600E}$ (Fig. 2i-b). On the other side, quinoline in general is a well-known as multi-kinase inhibitory scaffold such as in lenvatinib **5** which works by inhibiting several tyrosine kinase receptors, including VEGFR-1,2,3, FGFR-1,2,3,4, RET, and c-KIT [21]. Notably, the quinoline-bearing compounds

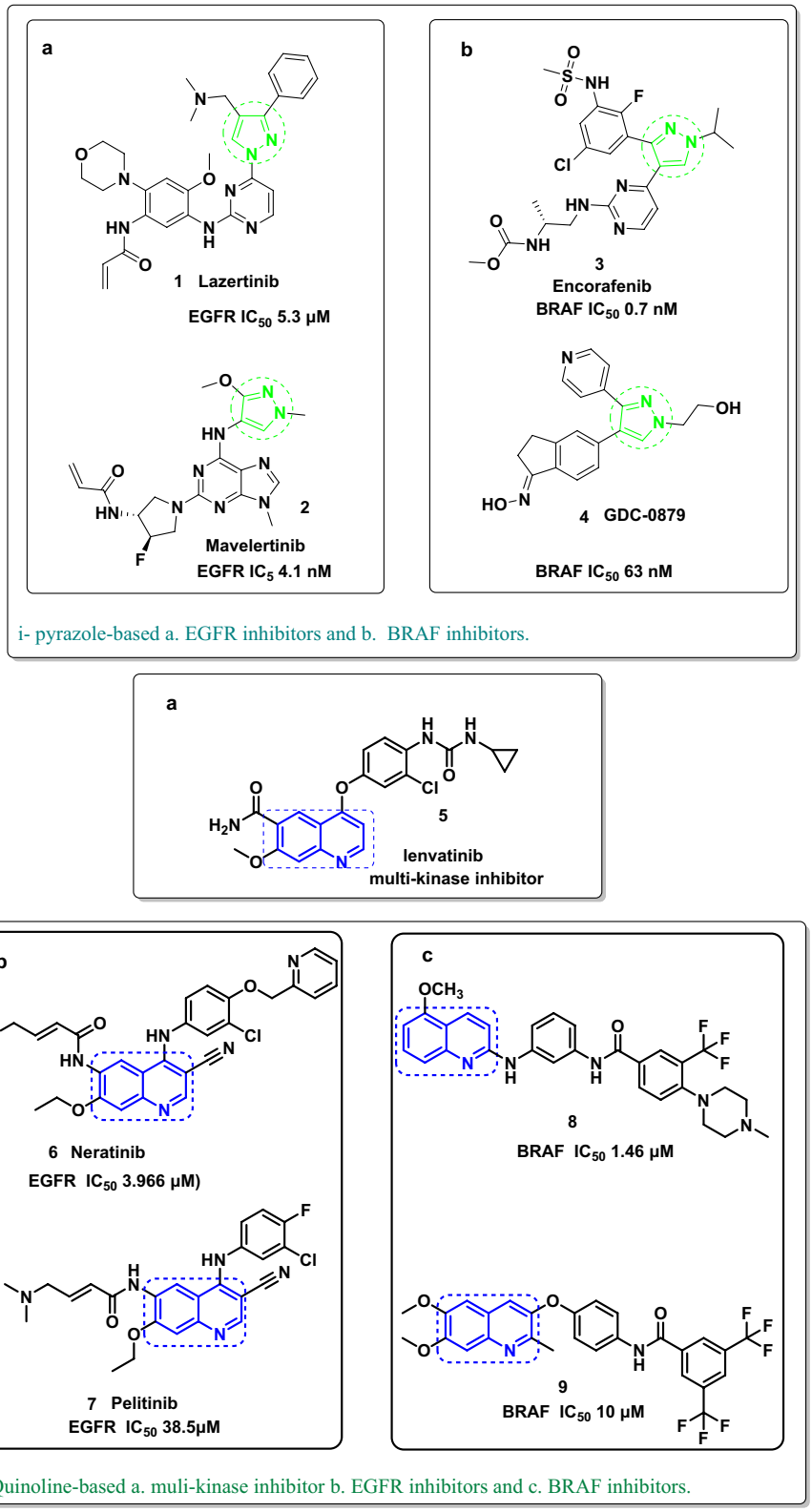
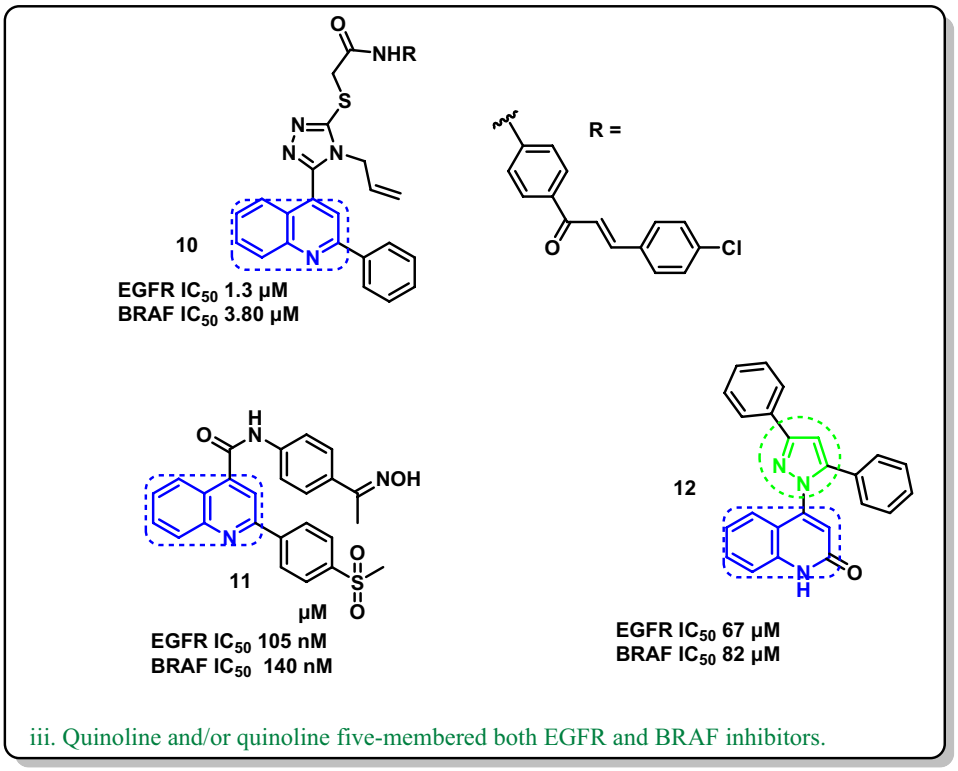


Fig. 2 Quinoline/or quinoline five-membered ring EGFR/BRAF single and/or dual mechanism

(Neratinib) **6** [22] (Pelitinib) **7** [23] were published as EGFR inhibitors (Fig. 2ii-a). Moreover, the quinoline-derived **8** and **9** [24] revealed $BRAF^{V600E}$ inhibitory activities (Fig. 2ii-b). In addition, the quinoline/triazole hybrid **10** [25] and the quinoline/amide-bridged **11** [26] showed promising dual inhibition of both the EGFR and $BRAF^{V600E}$ oncogenic

Fig. 2 (continued)



iii. Quinoline and/or quinoline five-membered both EGFR and BRAF inhibitors.

proteins. Further, as a possible twin inhibitory mechanism, the quinoline/pyrazole hybrid **12** [26] worked on both EGFR and $BRAF^{V600E}$ targets (Fig. 2iii). Therefore, searching for a hybrid of quinoline and pyrazole may be the shortest way to obtain a dual-mechanism anticancer.

Considering the Structure–activity relationship of the EGFR-TKIs [27] (Fig. 3); pelitinib, erlotinib [28], and neratinib could be summarized as follows: (a) the adenine pocket is occupied by a heteroaromatic scaffold; (b) a NH spacer that interacts with the amino acids inside the linker region; (c) a terminal hydrophobic moiety; and (d) a hydrophobic tail at the end that settles into the hydrophobic area. On the other hand, the requirements for $BRAF^{V600E}$ inhibitors such as Encorafenib, Dabrafenib [29], and Vemurafenib [30] could be encapsulated in (a) a sulfonamide moiety or alkylated sulfonamide moiety which is essential for interacting with the important amino acid residue; (b) a phenyl moiety occupies the extended side of the pocket; (c) C=O, pyrazole, or imidazole linker; and (d) heteroaromatic system like azaindole or pyrimidine (bioisosteric quinoline as represented in our target compounds) which occupied the adenine pocket. Consequently, considering the essential requirements for EGFR and $BRAF^{V600E}$ inhibitors and utilizing the bio versatility of both quinoline and pyrazole moieties, we designed a novel quinoline-pyrazole-based derivatives that have the main features and pharmacophores for both EGFR and $BRAF^{V600E}$ inhibitors such as a quinoline heteroaromatic system, modified NH linker, or spacer with hydrazone attached to the pyrazole and phenyl sulfonamide moiety.

Results and discussion

Chemistry

The intermediates 4-hydrazineylquinolin-2(1*H*)-one derivatives **1a–e** were synthesized according to the reported method [31].

The final compounds have been synthesized using the procedures outlined in Scheme 1. An equimolar amount of 2,4-pentanedione and *N,N*-dimethylformamidedimethyl acetal (DMF-DMA) was stirred overnight. Then, 4-hydrazineylquinolin-2(1*H*)-ones **1a–e** were added to form intermediates **2a–e** according to the proposed Michael-addition mechanism (Fig. 4) [32]. The final compounds **4a–j** were obtained by condensing acetyl pyrazolyl quinoline derivatives **2a–e** with phenyl hydrazine derivatives **3a-b**.

Along with the expected compounds, confirmatory ^{1}H NMR, ^{13}C NMR, and HRMS analyses were confirmed. Compound **4e**'s ^{1}H NMR revealed a set of twelve protons between 9.61 and 6.78 δ ppm that were related to aromatic and sulfonamide protons, two methyl groups in the aliphatic region, and one proton at 12.29 δ ppm that corresponded to the NH amidic. In addition to the precise number of carbons, ^{13}C NMR

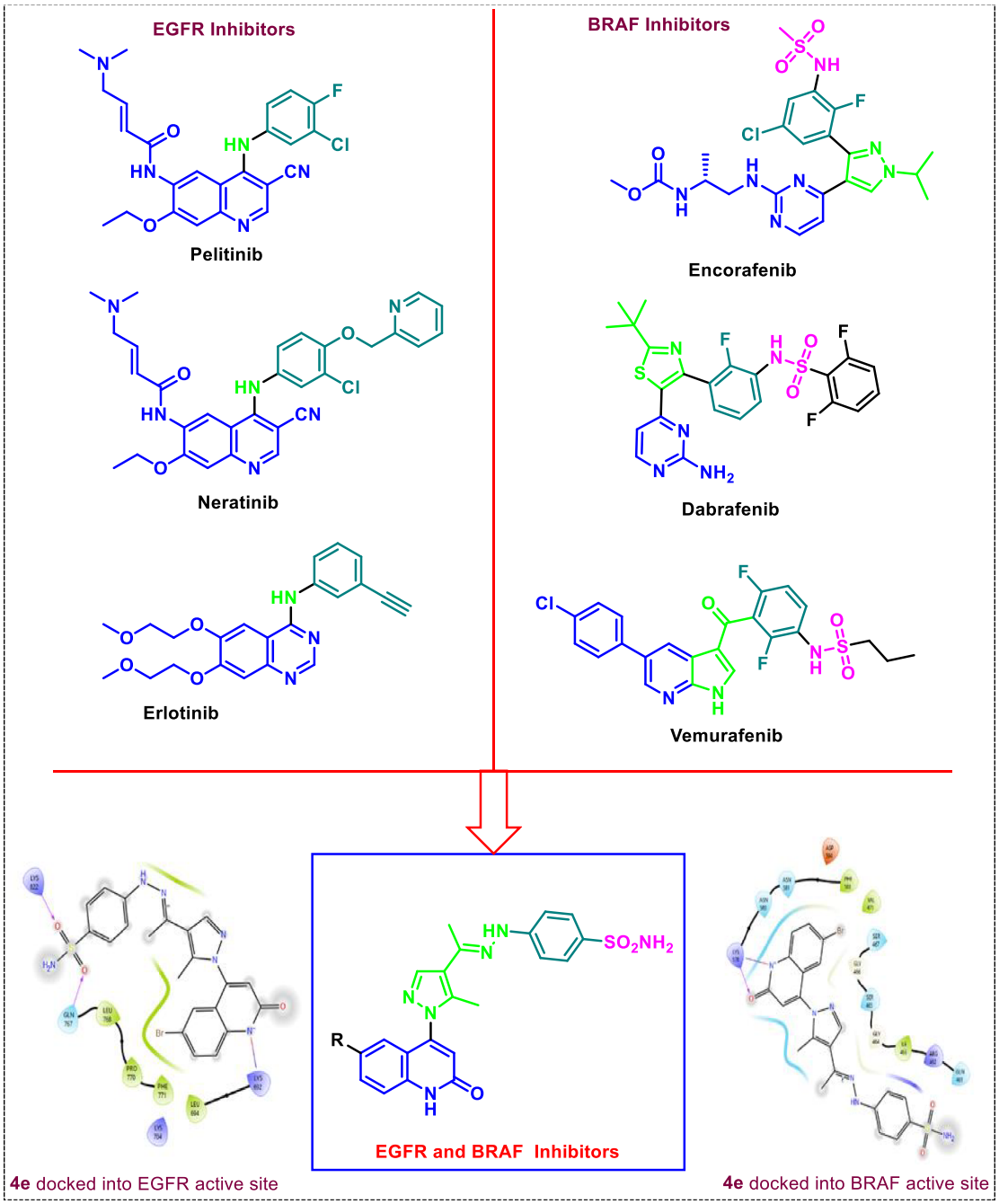
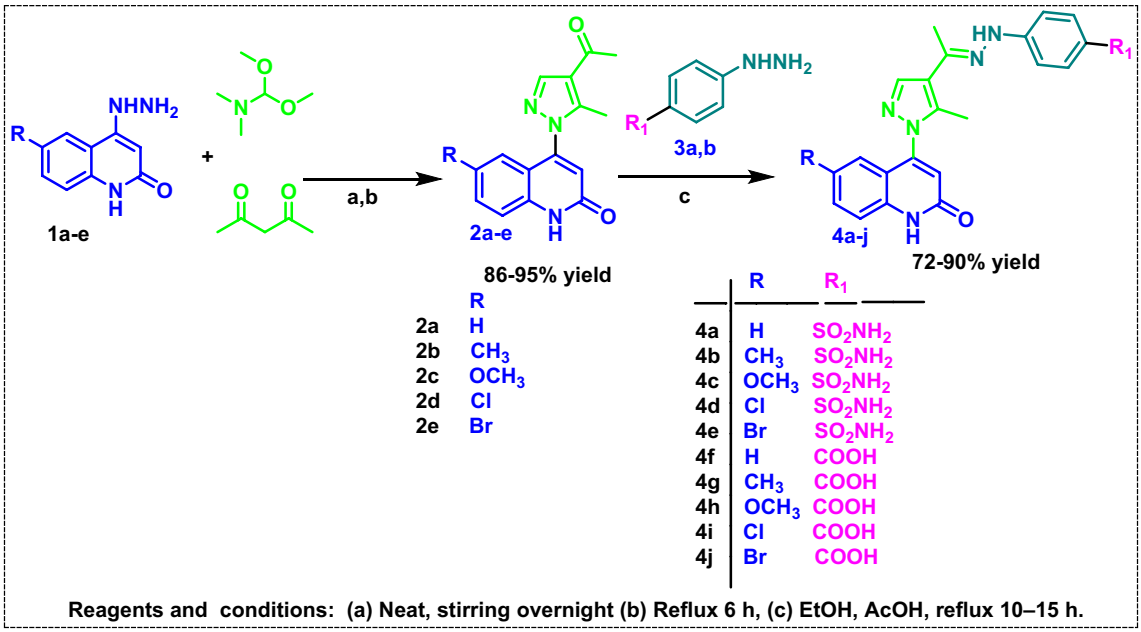


Fig. 3 Rationale design for the final compounds **4a–j** inspired from the reported EGFR and $BRAF^{V600E}$-active-marketed anticancer drugs

revealed two peaks in the aliphatic region that were ascribed to methyl carbons. Furthermore, compound **4e** showed molecular ion peaks at m/z 515.0499, which corresponds to its molecular formula conforming its purity.



Scheme 1 Synthetic approach to target compounds **4a–j**

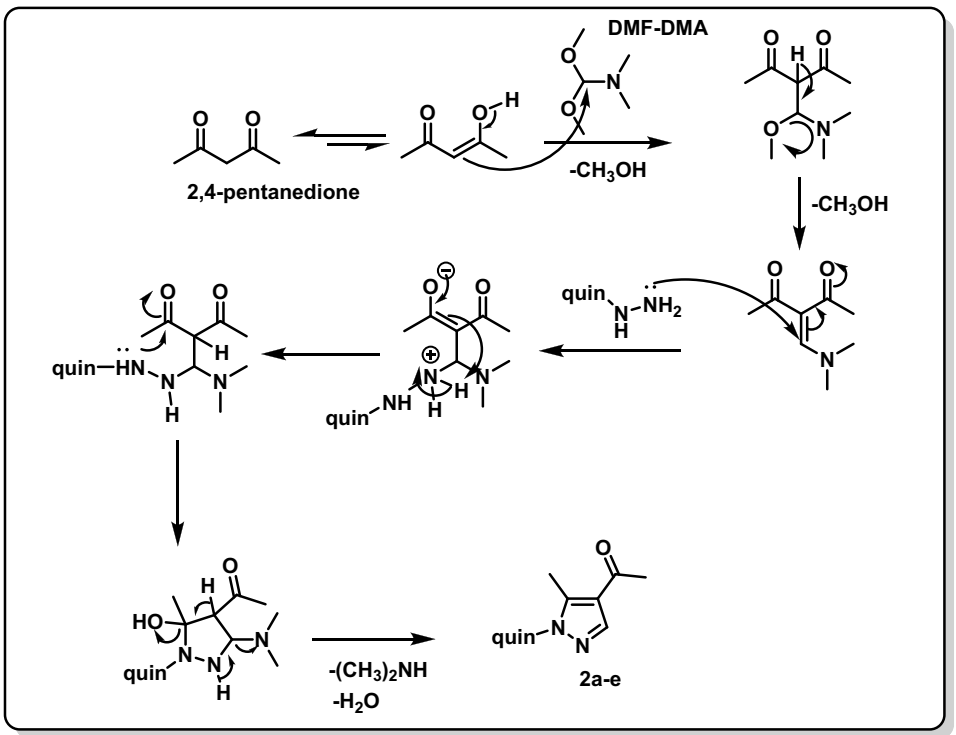


Fig. 4 The proposed Michael-addition mechanism for the synthesis of compounds **2a–e**

Biology

National Cancer Institute (NCI) screening

Ten final compounds **4a–j** and five intermediates **2a–e** have been selected by the National Cancer Institute (NCI) for anticancer screening over a panel of 60 cancer cells that cover a variety of histological tissues, including the central nervous system, leukemia, lung, colon, kidney, ovary, breast, and prostate, using the protocol established by the National Cancer Institute (NCI) [33]. In a primary screening, each compound was screened at a concentration of 10

Table 1 Heatmap diagram of NCI-60 inhibition by compounds 2a–e and 4a–j at 10 μM

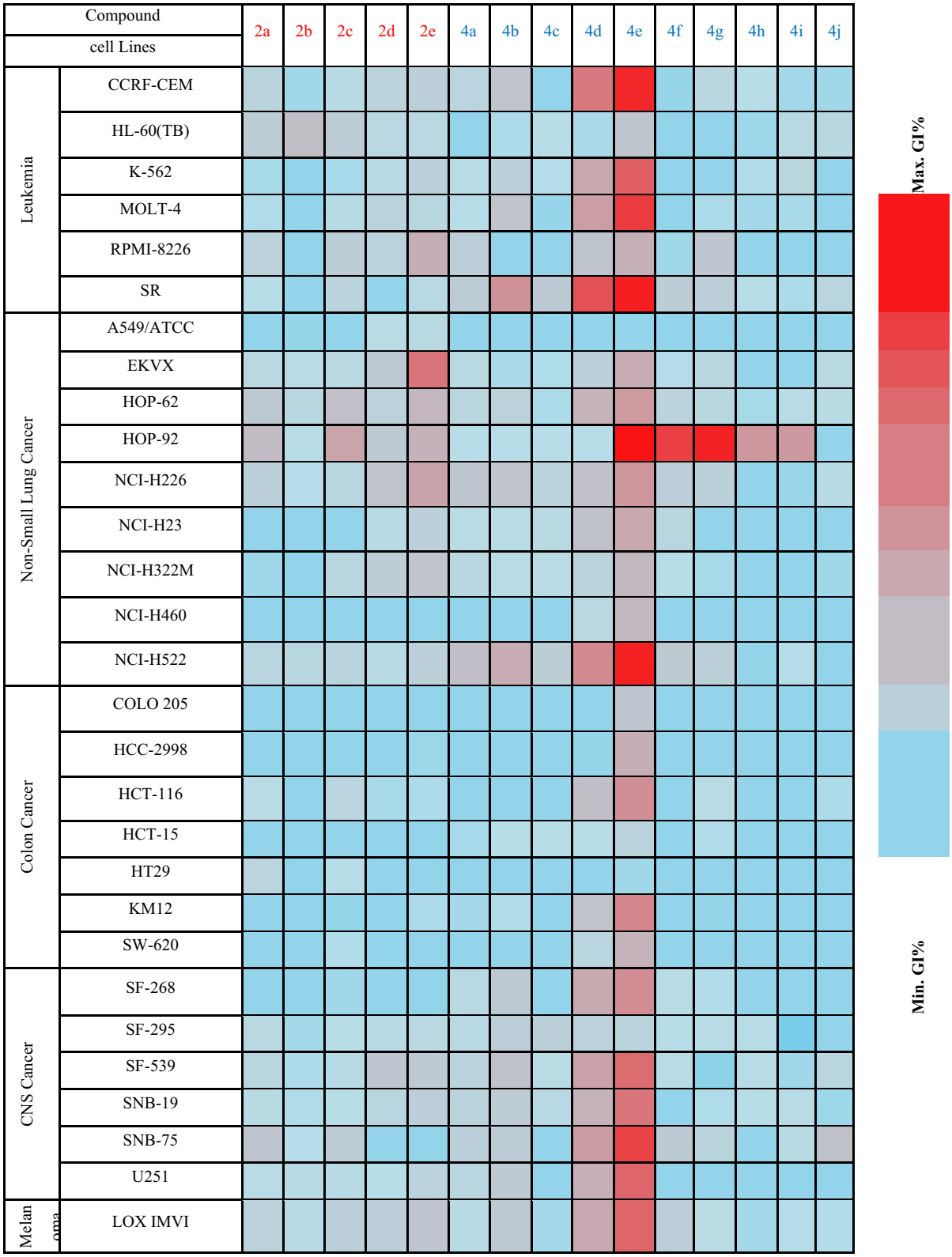
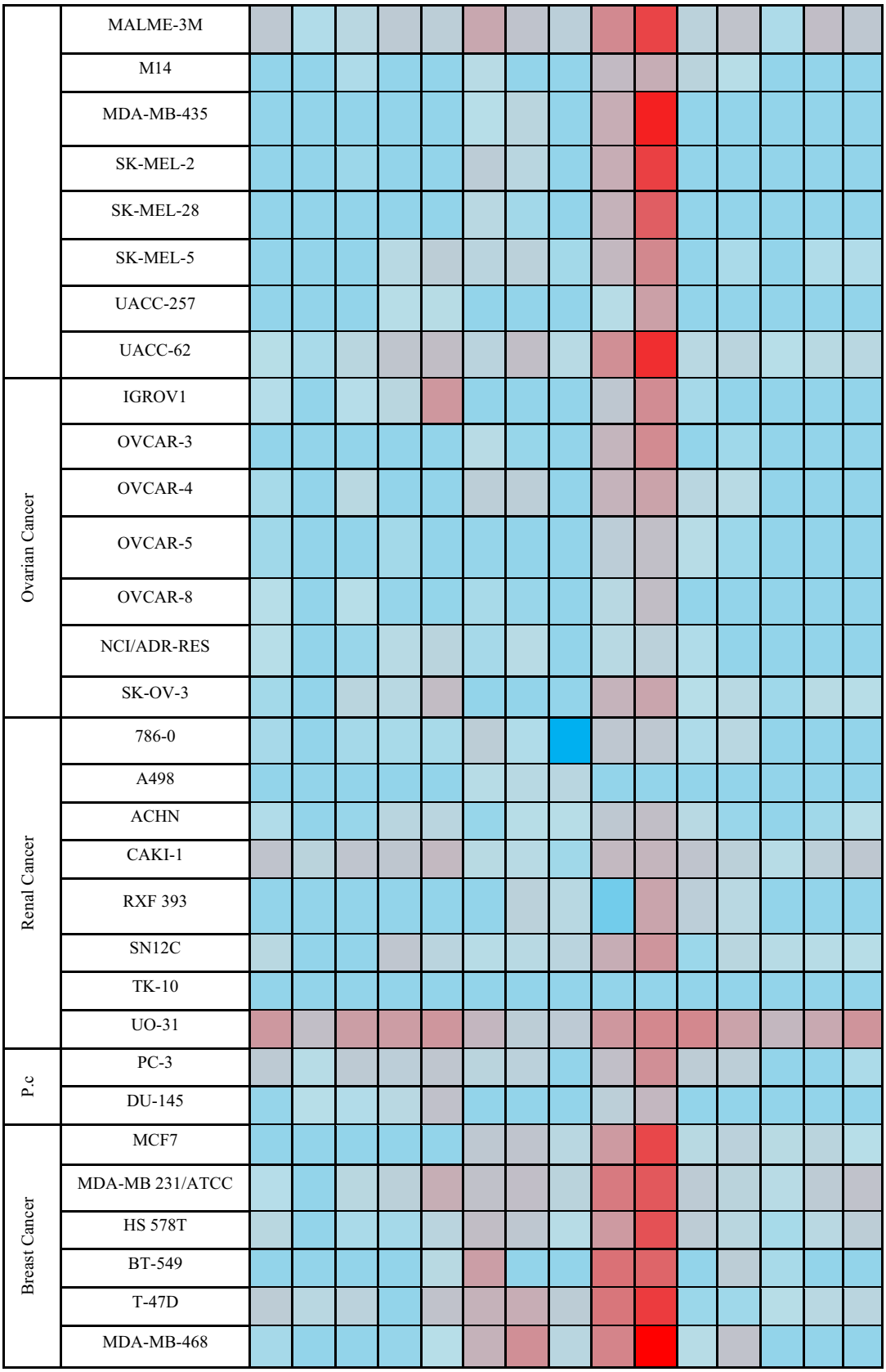


Table 1 (continued)

	MALME-3M
	M14
	MDA-MB-435
	SK-MEL-2
	SK-MEL-28
	SK-MEL-5
	UACC-257
	UACC-62
Ovarian Cancer	IGROV1
	OVCAR-3
	OVCAR-4
	OVCAR-5
	OVCAR-8
	NCI/ADR-RES
	SK-OV-3
Renal Cancer	786-0
	A498
	ACHN
	CAKI-1
	RXF 393
	SN12C
	TK-10
	UO-31
P.c	PC-3
	DU-145
Breast Cancer	MCF7
	MDA-MB 231/ATCC
	HS 578T
	BT-549
	T-47D
	MDA-MB-468



*p.c. prostate cancer

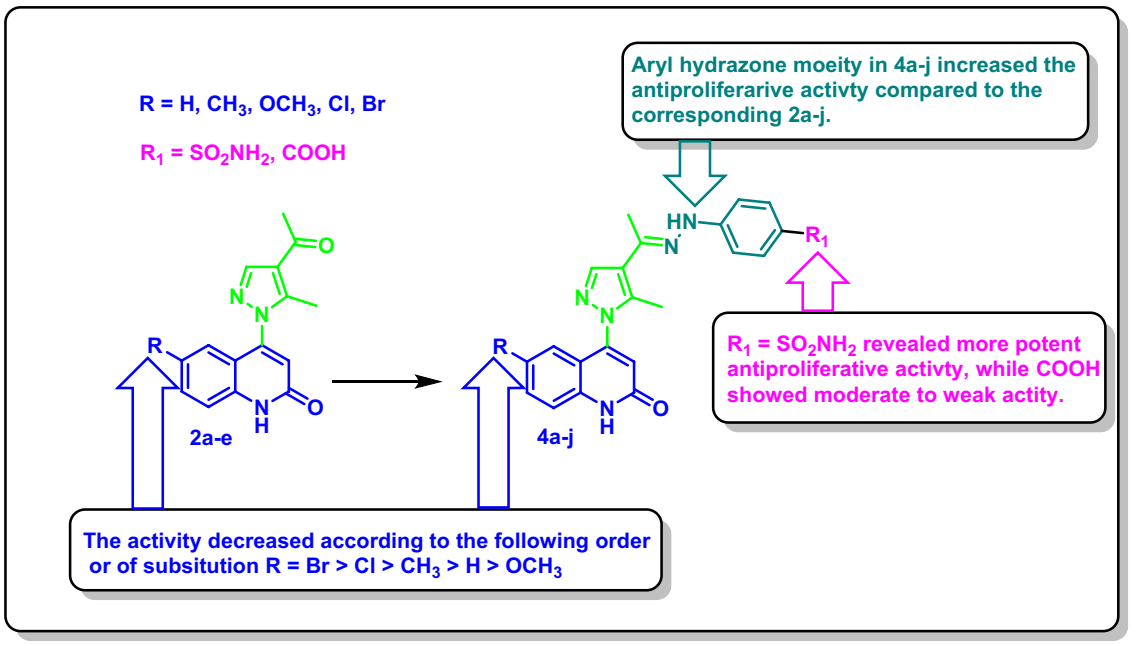


Fig. 5 Structure activity relationship (SAR) of **2a–e**, and **4a–j**

μM. The results were displayed in the supplementary data and expressed as the mean GI% of the treated cells relative to the control cells [34]. The following heatmap (Table 1) highlighted that compounds **4d–g** have promising activity on HOP-92 lung, MOLT-4 leukemia, and T-47D breast cell lines. Interestingly, compound **4e** showed remarkable activity over the most NCI cancer cell lines.

Structure activity relationship (SAR)

The data on in vitro NCI screening findings (Table 1) show above points to the following main trend: (a) regarding to the electron-donating groups, quinolin-2-one's activity was enhanced by halogen substitution on **C-6**. (b) The antiproliferative effect was more pronounced in the substituted phenyl hydrazone **4a–j** than in the acetylated intermediates **2a–j**. (c) Sulfonamide-substituted compounds **4a–e** are more active compared to the carboxylated compounds **4f–j** (Fig. 5).

Antiproliferative assay

To a greater extent, the MTT assay [35] was employed to assess the antiproliferative effect of the previously screened promising hybrids **4d–g**. The MTT assay results reassured the promising antiproliferative activity of compound **4e** on the three human cancer cell lines: leukemia (MOLT-4), lung cancer (HOP-92), and breast cancer (T47D) cell lines with mean inhibitory concentration $IC_{50} \pm SEM$ 8.62 ± 0.34, 4.982 ± 0.2, and 8.023 ± 0.31 μM, respectively, in comparison to the Staurosporine reference

Table 2 In vitro cytotoxicity of compounds **4d–g** on MOLT-4, HOP-92, and T47D cancer cell lines and cytotoxicity on the normal WI-38 cell line

Compound	Antiproliferative activity $IC_{50} \pm SEM$ (μM)			
	T-47D	HOP-92	MOLT-4	W1-38
4d	13.85 ± 0.48	36.52 ± 1.46	7.24 ± 0.29	62.46 ± 2.49
4e	8.62 ± 0.34	4.982 ± 0.2	8.023 ± 0.31	29.62 ± 1.18
4f	28.56 ± 0.99	24.93 ± 1.9	16.31 ± 0.65	42.14 ± 1.68
4g	9.71 ± 0.34	14.72 ± 0.66	6.17 ± 0.25	37.57 ± 1.5
Staurosporine	4.94 ± 0.19	3.172 ± 0.19	5.856 ± 0.23	17.54 ± 1.5

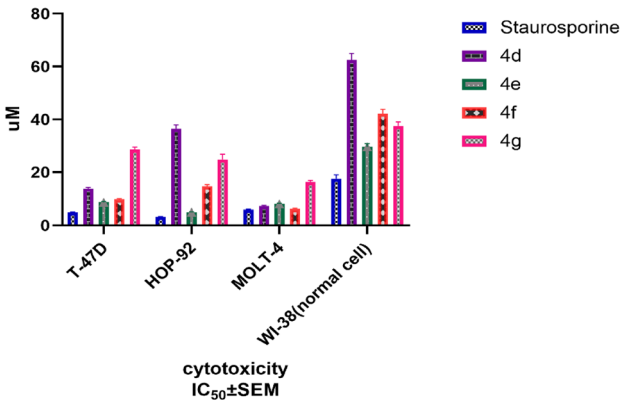


Fig. 6 In vitro cytotoxicity of compounds **4d–g** on MOLT-4, HOP-92, and T47D cancer cell lines and cytotoxicity on the normal WI-38 cell line

[36] (a broad-spectrum protein kinase inhibitor), which has $IC_{50} \pm SEM$ µM 4.94 ± 0.19, 3.172 ± 0.19, and 5.856 ± 0.23, respectively, on the same cell lines. Moreover, compound **4e** did not reveal significant cytotoxicity to the normal cell line WI-38, with $IC_{50} \pm SEM$ µM 29.62 ± 1.18 compared to the reference compound with $IC_{50} \pm SEM$ µM 17.54 ± 1.5 (Table 2, Fig. 6).

EGFR inhibitory activity

The inhibitory effect of the most potent antiproliferative derivatives **4d–g** was examined against EGFR as a potential molecular target. The compounds' IC_{50} values are shown in Table 3. The antiproliferative assay and this inhibitory assay produced identical results. As before, the most effective antiproliferative agent **4e** (R = Br, $R^1 = SO_2NH_2$) had an IC_{50} value of 0.055 ± 0.002 µM, which was much higher than the reference erlotinib IC_{50} of 0.06 ± 0.002 µM. According to these results, **4e** may be a potential EGFR inhibitor with antiproliferative activity, which supports our previous theory on the mechanism of action of **4e** (Table 3, Fig. 7). See Appendix B.

Table 3 The IC_{50} values of compounds **4d–g** against EGFR and $BRAF^{V600E}$

Compound	EGFR inhibition $IC_{50} \pm SEM$ (µM)	$BRAF^{V600E}$ inhibition $IC_{50} \pm SEM$ (µM)
4d	0.156 ± 0.006	0.249 ± 0.01
4e	0.055 ± 0.002	0.068 ± 0.003
4f	0.64 ± 0.023	0.410 ± 0.016
4g	0.194 ± 0.007	0.194 ± 0.008
Erlotinib	0.06 ± 0.002	ND
Vemurafenib	ND	0.035 ± 0.001

N.B: (ND) = Not Determined

$BRAF^{V600E}$ inhibitory activity

Using Vemurafenib as the control medication, Compounds **4d–g** were further assessed for their inhibitory activity against $BRAF^{V600E}$. Compounds **4d–g** showed moderate anti-$BRAF^{V600E}$ activity (IC_{50} values ranging from 0.194 ± 0.008 to 0.410 ± 0.016 µM) compared to Vemurafenib ($IC_{50} = 0.035 \pm 0.001$ µM). On the other hand, compound **4e**, with an IC_{50} of 0.068 ± 0.003 µM, was the most potent inhibitor of $BRAF^{V600E}$. These results imply that compound **4e** may act with dual inhibition for EGFR and $BRAF^{V600E}$ as an antiproliferative agent (Table 3, Fig. 7). See Appendix B.

Cell cycle analysis

Research has been done on how the most powerful antitumor compound, **4e**, affects the HOP-92 cell cycle's growth and apoptosis. HOP-92 cells were treated for 24 h at an IC_{50} value of **4e** (4.982 µM). The results of the study (Table 4, Fig. 8) reveal that a higher apoptosis rate at the pre-G1 phase for compound **4e** on HOP-92 with a percent of cell accumulation of 54.11% indicates that cell growth is arrested at the G1 phase. In S and G2/M phases, an unnoticeable change percent of cell accumulation was observed in HOP-92 treated with **4e** (31.3%) and (14.6%), respectively (Table 4).

Table 4 Cell cycle analysis of compound **4e** in the HOP-92 cancer cell line

		DNA content			Comment
	IC_{50} µM	% G0–G1	% S	% G2/M	
4e/HOP-92	4.98	54.11	31.3	14.6	Cell growth arrest at G1phase
Cont. HOP-92	–	48.26	35.7	16.08	

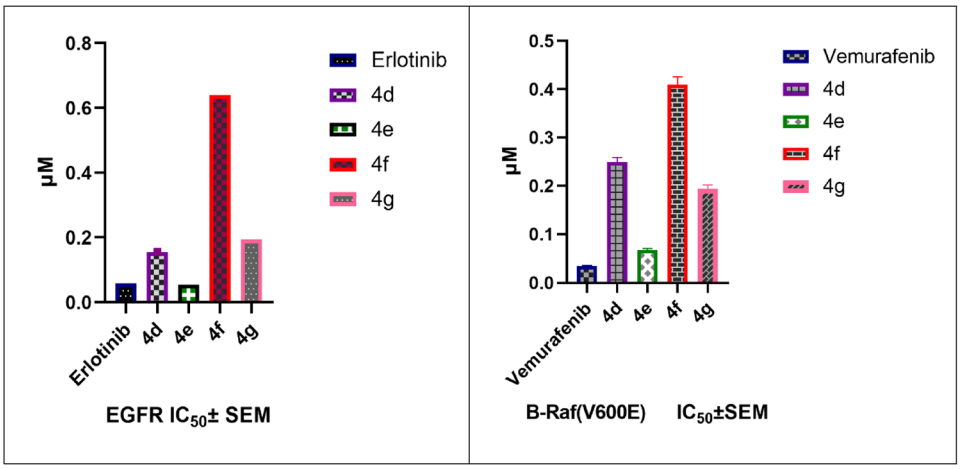


Fig. 7 The IC_{50} values of compounds **4d–g** against EGFR and $BRAF^{V600E}$

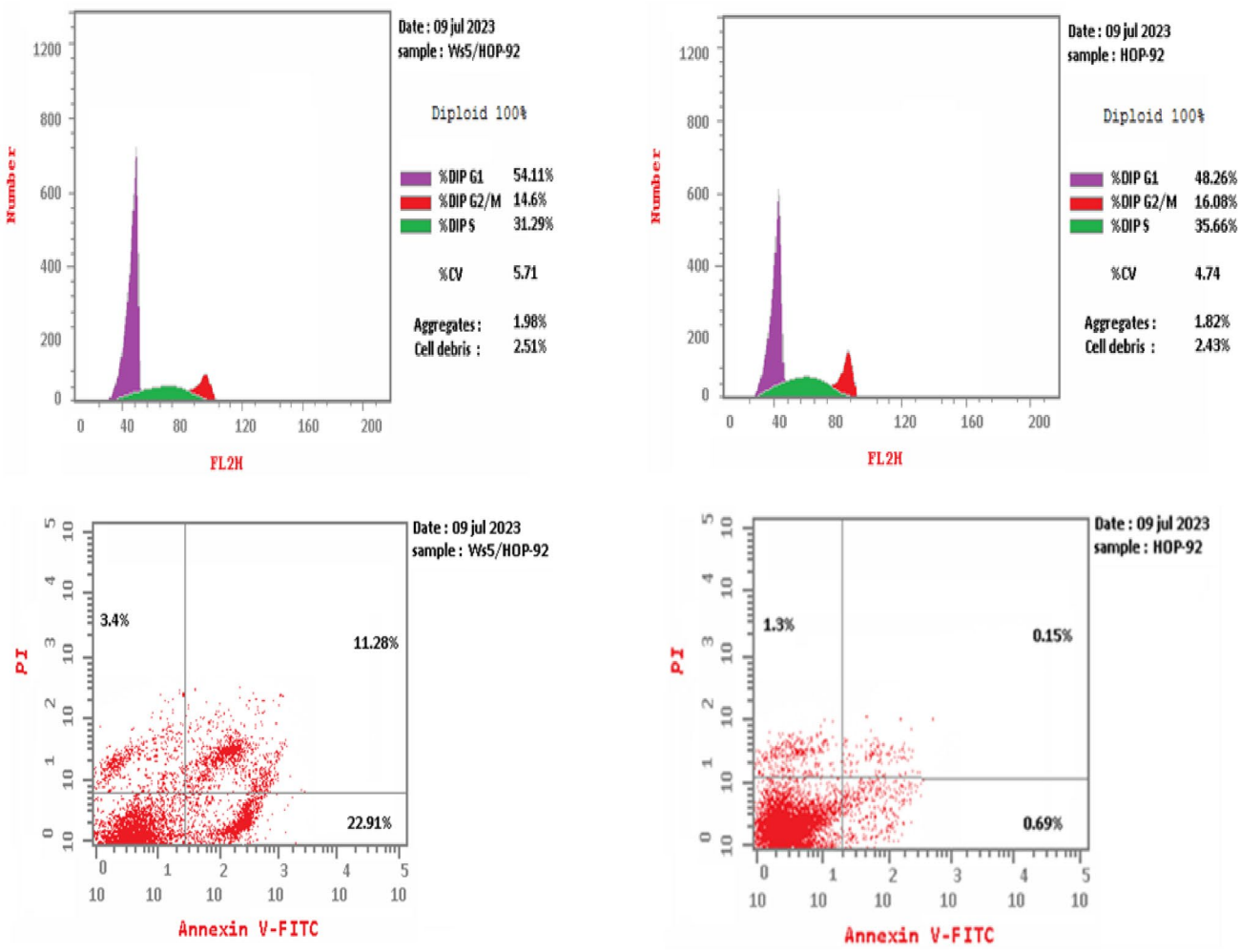


Fig. 8 Cell cycle analysis and apoptosis detection of **4e** in HOP-92 cancer cell line

Apoptosis assay

Using the Annexin V-FITC/PI test [37], the tendency of compound **4e** to cause apoptosis and its potential association with cytotoxic action were evaluated. The cells were labeled with annexin V-FITC/PI and cultured for 24 h to detect any signs of apoptosis. The HOP-92 cell cycle analysis revealed that **4e** treatment was followed by pre-G1 apoptotic signaling. According to research on early and late apoptosis and DNA content (Figs. 9, 10), **4e** with 3.4% necrosis is probably going to result in a large amount of apoptosis (Table 5 and Fig. 10).

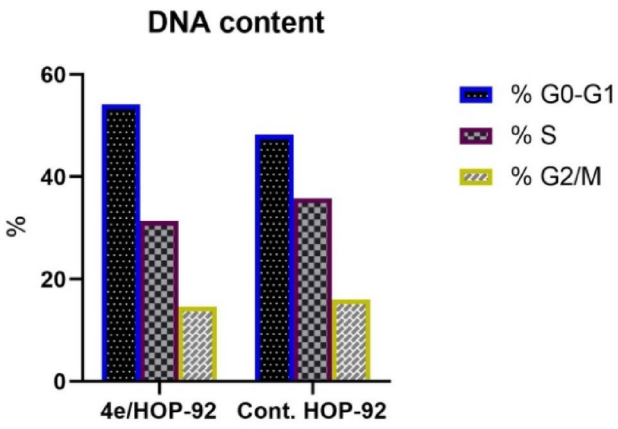


Fig. 9 DNA content of **4e** in the HOP-92 cancer cell line

Apoptotic indicators

In the depicted findings, compound **4e** affected Bcl-2, caspase-3, and caspase-9, increasing the expression of caspase-3/9 and decreasing the expression of Bcl-2, confirming the apoptotic status [27]. Compound **4e** was found to increase the levels of several mitochondrial apoptotic proteins, such as the main executioner protease (caspases-3/-9)

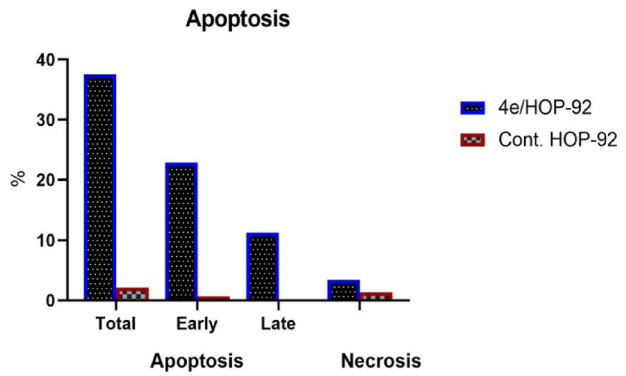


Fig. 10 Apoptosis detection of **4e** in the HOP-92 cancer cell line

Table 5 Apoptosis detection of **4e** in the HOP-92 cancer cell line

	Conc	Apoptosis			Necrosis
	IC_{50} µM	Total	Early	Late	
4e/HOP-92	4.982	37.59	22.91	11.28	3.4
Cont. HOP-92	–	2.14	0.69	0.15	1.3

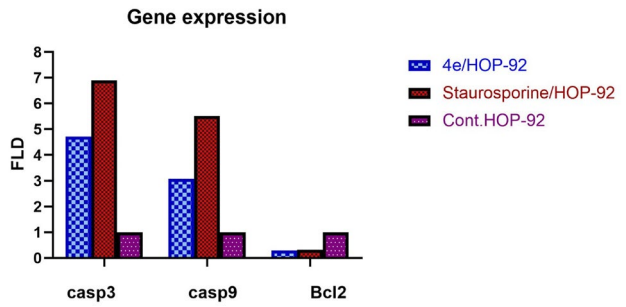


Fig. 11 Effect of **4e** on Bcl-2, Caspases-3, and Caspases-9 levels inside the HOP-92 cells

and anti-apoptosis marker (Bcl-2). The results displayed in Fig. 11 showed that the levels of caspases-3 and -9 in HOP-92 cells treated with **4e** were greater than those in the untreated control group by 4.716 and 3.082-fold, respectively (Table 6, Fig. 11). On the other hand, in comparison to the untreated reference, **4e** administration of HOP-92 successfully decreased expression of the anti-apoptotic Bcl-2 protein to one third.

In silico studies

Docking analyses of the most stable poses of quinolone-based hybrids **4d–g** along with the selected reference ligands erlotinib and vemurafenib were accomplished against EGFR and $BRAF^{V600E}$-active sites.

Table 6 Effect of 4e on Bcl-2, Caspases-3, and Caspases-9 levels inside the HOP-92 cells

RT-PCR Fold Change		FLD		
Code	IC_{50}	Casp-3	Casp-9	Bcl-2
4e/HOP-92	4.982	4.716	3.082	0.299
Staurosporine/HOP-92	3.172	6.906	5.514	0.326
Cont.HOP-92	–	1	1	1

Molecular docking simulation of the quinolone-based hybrids 4d–g inside the EGFR-active site

Believing on, the EGFR kinase domain (EGFRK) adopts an NH2-terminal lobe (N-lobe) that is mainly composed of β-strands and one α-helix (αC), and larger COOH terminal lobe (C-lobe) that is typically α-helical. Moreover, researchers have discovered that a cleft, which divides the two lobes, combines ATP, ATP analogs, and ATP-competitive inhibitors [38, 39]. Also considering that, the ATP-binding pocket at the intermediate cleft is divided into three main binding regions: (1) The adenine region, or hinge region, where the adenine free amino group accommodates the H-bond donor effect with the Gln767 residue, and the adenine N1 position establishes H-bond acceptor effect with the neighboring Leu768 and Met769 residues, (2) The sugar region: where the ATP ribose is located and H-bonded by its hydroxyl groups with the Asp86 residue, and (3) the phosphate-binding region: where the triphosphate part of the ATP converges and is H-bonded to the crucial Lys33 and Asp145 amino acids [40, 41]. Consequently, all the reported EGFR inhibitors, such as 4-aminoquinazolines [42], pyrido[2,3-d]pyrimidines [43], and pyrrolo[2,3-*b*]pyridine [44, 45], have been counted as competitive inhibitors at the ATP-binding pocket, especially at the ATP-hinge region. Herein, we accomplished a molecular docking simulation of the reference drug erlotinib as a sort of 4-aminoquinazoline inhibitor [46] and the novel quinolone-based hybrids 4d–g to validate their relative affinity against the EGFR-active site. The reference erlotinib exerted a glide score of ($S = -2.485$ kcal/mol) that could be attained through worthy H-bonding acceptor interactions of its ether oxygen with the Lys851 amino acid (1.83 A°) and the N1 position of the quinazoline ring with the Lys721 residue (2.31 A°). In addition to a precious pi-pi stacking with the Phe699 amino acid (4.35 A°). Fortunately, all the investigated quinolone-based hybrids 4d–g exhibited superior glide scoring than the reference drug erlotinib, whereas compound 4d ($S = -3.483$ kcal/mol) utilizes its sulfonamide moiety to reveal two H-bond acceptor effects with Lys822 and the critical Gln767 amino acids, along with a prominent H-bond of the N1 position of the 2-quinolone ring with the key Lys692 (3.10 A°). Providently, comparable with the in vitro assay IC_{50} results, the sulfonamide-bearing compound **4e** that

Table 7 Docking scores (kcal/mol) and the key involved residues in the interactions of the investigated compounds **4d, 4e, 4f, 4g**, and the reference drug erlotinib, accompanied with their bond length values (A°) inside the EGFR-active site (PDB ID: 1M17)

Compound	Glide score (kcal/ mol)	H-bond	H-bond length (A°)	Salt bridge	Salt bridge length (A°)	Pi-pi stacking	Pi-pi stacking length (A°)
4d	−3.483	Lys692 (1)	3.10	–	–	–	–
		Gln767 (1)	2.02				
		Lys822 (1)	2.47				
4e	−3.226	Gln767 (1)	2.06	Lys692 (1)	3.14	–	–
		Lys822 (1)	2.57				
4f	−4.407	Lys692 (1)	1.82	Lys822 (1)	4.26	–	–
		Gln767 (1)	1.82				
4g	−3.806	Lys704 (1)	2.37	Lys822 (1)	4.62	–	–
		Lys822 (1)	1.66				
Erlotinib	−2.485	Lys851 (1)	1.83	–	–	Phe699 (1)	4.35
		Lys721 (1)	2.31				

accomplished the EGFR inhibitory effect of (0.055 µM) in Table 7 achieved glide scoring of (3.226 kcal/mol) through performing two H-bond acceptor interactions with the same residues Lys822 and Gln767 that interact with compound 4d. Nevertheless, it accommodates a valuable salt bridge with the crucial residue Lys692 (3.14 A°) (Table 7, Fig. 12). Also, the novel carboxy-bearing candidates 4f ($S = -4.407$ kcal/mol) and 4g ($S = -3.806$ kcal/mol) performed obvious salt bridges with the Lys822 residue due to their carboxylate oxygen, while compound 4f elucidated two H-bond acceptor interactions of the same bond length (1.82 A°) with the Lys692 and Gln767 residues due to its 2-quinolone carbonyl and carboxylate carbonyl, respectively.

Meanwhile, compound 4g also clarified also two H-bond acceptor interactions with Lys704 (2.73 A°) and Lys822 (1.66 A°) due to the N2 of its pyrazole core and the carbonyl oxygen of its carboxylate, respectively (Table 7, Fig. 12). Wherefore, compound **4e**-bearing pyrazole could be considered a promising EGFR inhibitor through ATP-competitive inhibition at the hinge region while it accommodates valuable contacts with Gln767 where the adenine part of ATP binds, and gaining a superior computational docking score and in vitro IC_{50} results over the reference erlotinib that requires further study.

Molecular docking simulation of the quinolone-based hybrids 4d–g inside the $BRAF^{V600E}$-active site

As the $BRAF^{V600E}$, within the mitogen-activated protein kinase (MAPK) signaling pathway, tends to be mutated in a significant number of cancers, particularly in about 50% of melanomas [47]. About 90% of $BRAF^{V600E}$ homo- and heterodimer mutations correlated with cancer contain a distinct mutation of the Val600 residue to Glu600 ($BRAF^{V600E}$), which prompts an active conformation without activation loop phosphorylation [48]. Therefore, approximately all patients promote drug resistance within about 6 months of treatment by $BRAF^{V600E}$ inhibitors that predominantly arise through reactivation of the MAPK pathway that is called transactivation [49]. In the present work, we investigated vemurafenib reference drug [50] besides the quinolone-based hybrids **4d–g** as chemically linked kinase inhibitors aiming to lock the $BRAF^{V600E}$ dimers in an inactive conformation that cannot endure transactivation and, hence, confirm their potential against mutated instances (Table 8, Fig. 13). The reference compound vemurafenib elucidated a useful glide score of (−3.266 kcal/mol), represented by four protruding H-bonding interactions with the Asn580, Arg575, Ser616, and Lys578 residues with bond lengths of 1.99, 2.33, 2.56, and 2.27 A°, respectively. In addition to a prominent salt bridge of sulfonamide nitrogen with the Lys578 amino acid and *pi*-cation interaction with the Lys601 besides the mutated Val600 residue. Fortunately, all the inspected quinolone-based hybrids **4d–g** revealed better glide scoring than the reference vemurafenib. While compound 4d sulfonamide oxygen created an H-bond acceptor effect with the Gln461 residue (2.13 A°), along with another H-bond acceptor effect of the N_2 of the pyrazole moiety with the Ser465 residue (2.43 A°), and a characteristic salt bridge of the 2-quinolone nitrogen with the crucial Lys578 residue to achieve a glide score of (−4.045 kcal/mol). Moreover, the sulfonamide compound **4e** that accomplished the most hopeful IC_{50} result among the investigated compounds (0.068 µM) displayed a glide score of (−3.474 kcal/mol) through an obvious H-bond acceptor interaction of its 2-quinolone carbonyl oxygen with the key Lys578 and a prominent salt bridge of its 2-quinolone nitrogen with the same residue. Also, the carboxy compounds **4f** and **4g** presented superior glide scoring over the reference vemurafenib of (−5.717 kcal/mol) and (−4.815 kcal/mol), respectively. Whereas compound **4f** demonstrated a useful H-bond donor effect of its 2-quinolone nitrogen with the Asn580 residue (2.21 A°), the 2-carbonyl oxygen protruded H-bond acceptor effect with the Ser536 amino acid

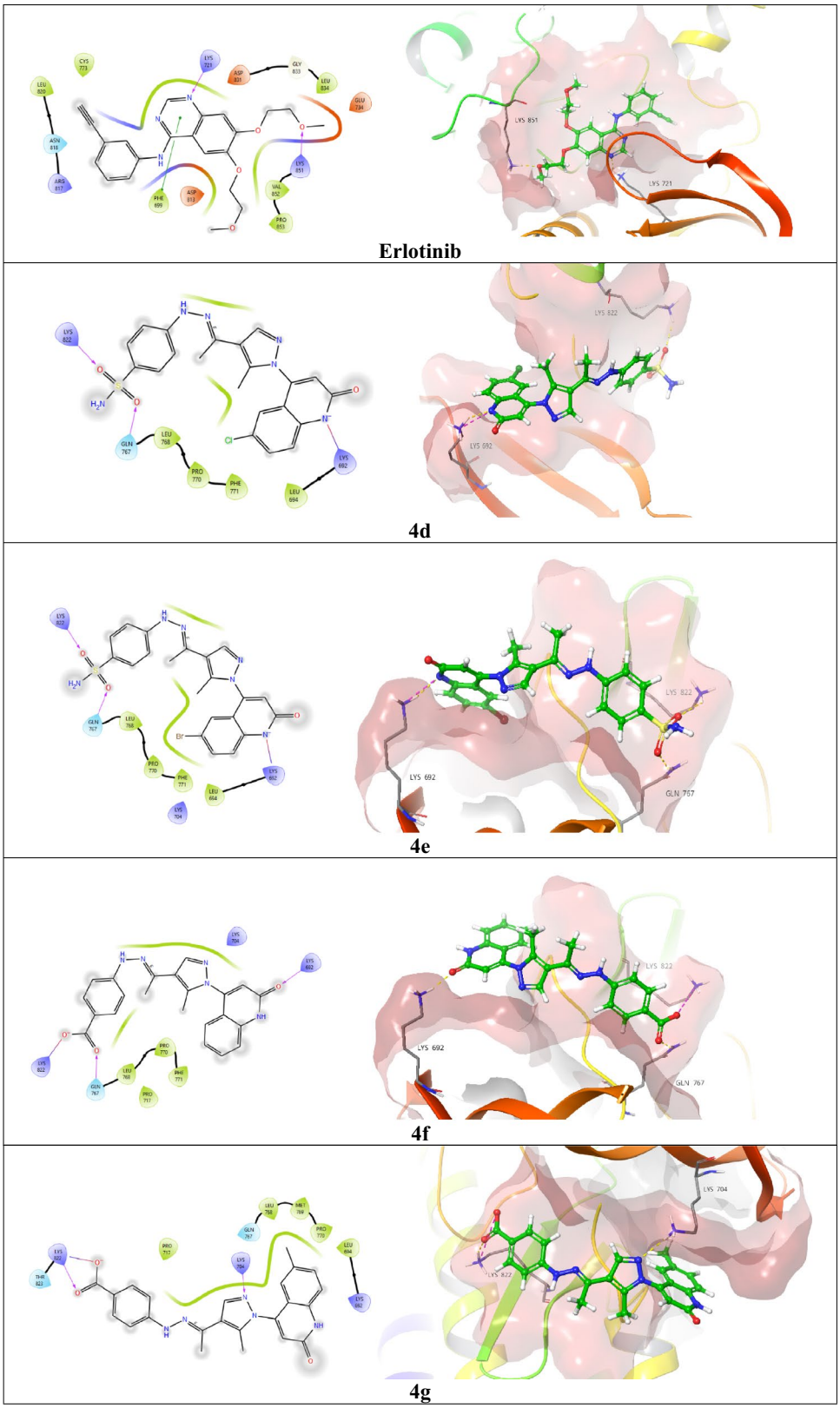


Fig. 12 Two-dimensional and three-dimensional (green ball and sticks) surface representation of the novel investigated quinolone-based hybrids **4d–g** besides the reference compound erlotinib in the active site of EGFR

Table 8 Docking scores (kcal/mol) and the key involved residues in the interactions of the investigated quinolone-based hybrids **4d–g** and the reference drug vemurafenib, accompanied with their bond length values (A°) inside the $BRAF^{V600E}$-active site (PDB ID: 5JRQ)

Compound	Glide score (kcal/ mol)	H-bond	H-bond length (A°)	Salt bridge	Salt bridge length (A°)	Pi-cation interaction	Pi-cation bond length (A°)
4d	−4.045	Ser465 (1)	2.43	Lys578 (1)	3.45	–	–
		Gln461 (1)	2.13				
4e	−3.474	Lys578 (1)	2.66	Lys578 (1)	3.56	–	–
4f	−5.717	Asn580 (1)	2.21	–	–	–	–
		Ser536 (1)	2.15				
4g	−4.815	Ser465 (1)	2.53	–	–	–	–
		Gln461 (1)	461				
Vemurafenib	−3.266	Asn580 (1)	1.99	Lys578 (1)	4.26	Lys601	6.51
		Arg575 (1)	2.33				
		Ser616 (1)	2.56				
		Lys578 (1)	2.27				

(2.15 A°). In a diverse manner, compound **4g** elucidated two H-bond acceptor effects due to its carboxylate carbonyl oxygen and N_2 of the pyrazole core with Gln461 (1.95 A°) and Ser465 (2.53 A°), respectively. Lastly, the inspected quinolone-based hybrids **4d–g** exposed superior binding affinity to the $BRAF^{V600E}$-active site that exceeds the reference drug vemurafenib that may explain their capability to overcome the mutated consequences of the $BRAF^{V600E}$ and treat the resistant malignant cases that require further investigation.

Pharmacokinetic profile (ADME) and drug-likeness

The online SwissADME tool [51] was used to calculate the expected physicochemical considerations. The obtained results provide a favorable impression of the unique synthesized candidates' feasibility profiles. It seems that none of the produced compounds violate the Lipinski criteria. Pharmacokinetic analysis revealed that compounds **4d** and **4e** have limited gastrointestinal (GI) absorption, which is regarded as a crucial factor for oral delivery. Compounds **4f** and **4g**, on the other hand, had substantial GI absorption (Table 9, Fig. 14). The Synthetic accessibility (SA) value is crucial when examining medicinal chemistry; the values acquired increase in difficulty from 1 to 10, which they cannot surpass. Thankfully, it was discovered that every produced molecule had values between 3 and 4, with no compound approaching or surpassing 10. In summary, all the compounds have suitable physicochemical parameters to be drug candidates [52].

Conclusion

A series of new compounds based on quinoline have been designed, synthesized, and tested for their ability to inhibit cell division. A panel of sixty cancer cell lines from the NCI was used to examine the newly produced compounds in vitro. Quinolone-based hybrids **4d–g** showed encouraging antiproliferative activity in the MTT experiment when compared to Staurosporine, the positive control. Compound **4e** was found to be the most effective; it may target EGFR and/or $BRAF^{V600E}$ to function as an antiproliferative agent. Compound **4e** displayed cell cycle arrest at the G0-1 phase and caused apoptosis against $BRAF^{V600E}$ and EGFR, two potential dual targets for anticancer therapy.

Regarding the molecular docking studies, quinolone-based hybrids **4d–g** clearly showed significant docking scores for EGFR and $BRAF^{V600E}$ in relation to the ligands vemurafenib and erlotinib, respectively. Interestingly, compound **4e** may prove to be a promising inhibitor for both the $BRAF^{V600E}$ and EGFR targets following structural alteration.

Experimental

Chemistry

General details: See Appendix A

General synthetic procedure for 4-(4Aacetyl-5-methyl-1H-pyrazol-1-yl)-6-substituted quinolin-2(1H)-one derivatives. (2a–e)

A mixture of 2,4-Pentanedione (5.0 mmol) was mixed with *N,N*-dimethylformamide-dimethyl acetal (DMF-DMA) (6.0 mmol) and was stirred overnight at room temperature. Next, a 4-hydrazineylquinolin-2(1*H*)-one derivative (5 mmol) was added, and the reaction mixture was heated at 70–80 °C in ethanol for 6 h. The reaction mixture was subsequently allowed to cool and refrigerated for 24 h. Then the reaction mixture was filtrated and washed with ethanol.

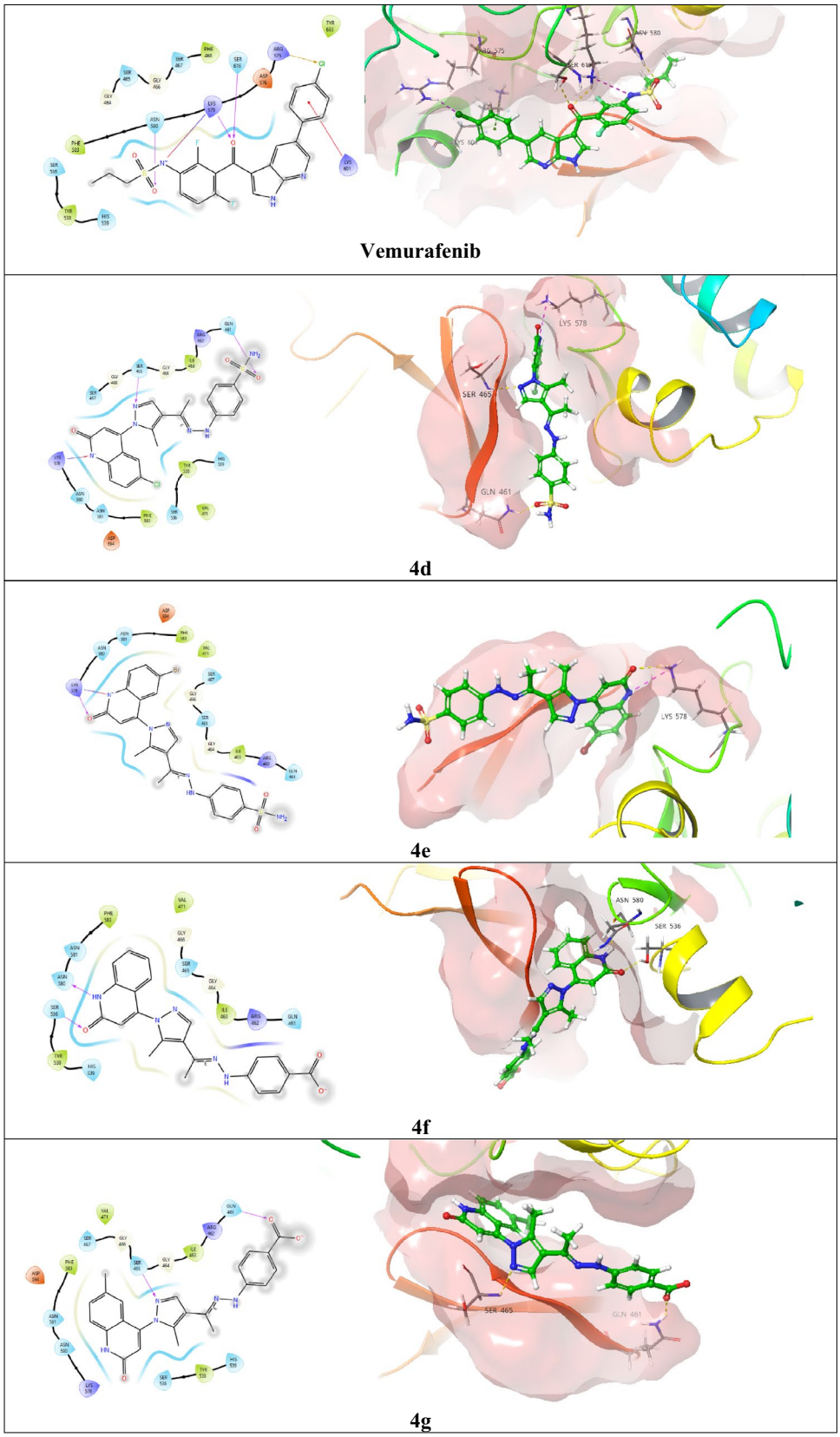


Fig. 13 Two-dimensional and three-dimensional (green ball and sticks) surface representation of the novel investigated quinolone-based hybrids **4d–g** besides the reference compound vemurafenib in the active site of $BRAF^{V600E}$

Table 9 Predicted ADME parameters of the novel compounds **4d–4g**

Comp.	Physicochemical properties					Pharmacokinetics		Drug likeness		Medicinal chemistry
	HBA[a]	HBD[b]	TPSA[c]	LogPo/w[d]	LogS[e]	GIA	Log Kp[f]	Lipinski	Vio[g]	SA
4d	6	3	143.61	2.66	−4.46	Low	−7.43	Yes	0	3.39
4e	6	3	143.61	2.74	−4.73	Low	−7.65	Yes	1	3.41
4f	5	3	112.37	2.72	−4.27	High	−6.77	Yes	0	3.23
4g	5	3	112.37	3.07	−4.57	High	−6.60	Yes	0	3.36

[a]: Number of hydrogen bond acceptors. [b]: Number of hydrogen bond donors. [c]: Topological polar surface area.[d]: Partition coefficient (lipophilicity). [e]: Water Solubility. [f]:(skin permeation). [g]: violation

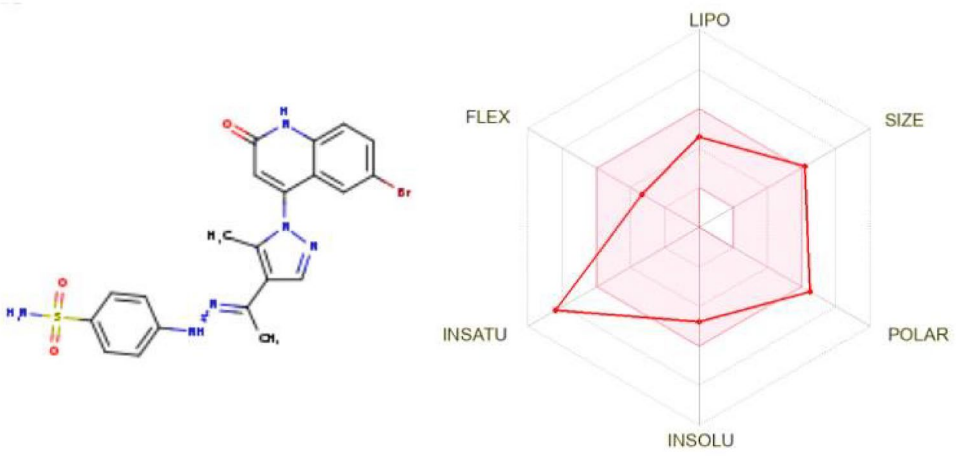


Fig. 14 Pharmacokinetic profile (ADME) and drug-likeness of compound **4e**

4-(4-Acetyl-5-methyl-1H-pyrazol-1-yl)quinolin-2(1H)-one (2a) Pale yellow powder, Yield: (93%); mp: 219–221 °C, ^{1}H NMR (400 MHz, DMSO-d_6) δ (ppm): 12.22 (1H s, 1H, NHCO), 8.38 (s, 1H), 7.60 (t, J = 7.7 Hz, 1H),7.44 (d, J = 8.2 Hz, 1H), 7.17 (t, J = 7.6 Hz, 1H), 6.96 (d, J = 7.5 Hz, 1H), 6.75 (s, 1H), 2.49 (s, 3H, –CH_3), 2.43 (s, 3H, –CH_3). ^{13}C NMR (100 MHz, DMSO-d_6) δ (ppm): 193.10, 161.29, 145.29, 144.03, 142.94, 139.33, 131.76, 123.99, 122.53, 120.62, 120.54, 116.36, 115.83, 28.85, 11.36. Anal. Calcd. For $C_{15}H_{13}N_3O_2$: C, 67.40; H, 4.90; N, 15.72. Found: C, 67.62; H, 5.06; N, 15.89.

4-(4-Acetyl-5-methyl-1H-pyrazol-1-yl)-6-methylquinolin-2(1H)-one (2b) Yield: (88%); mp: 223–225 °C, ^{1}H NMR (400 MHz, DMSO-d_6) δ (ppm): 12.15 (s, 1H, NHCO), 8.38 (s, 1H), 7.43 (d, J = 8.4 Hz, 1H), 7.35 (d, J = 8.4 Hz, 1H), 6.76 (s, 1H), 6.70 (s, 1H), 2.49 (s, 3H, –CH_3), 2.42 (s, 3H, –CH_3), 2.25 (s, 3H, –CH_3 ^{13}C NMR (100 MHz, DMSO-d_6) δ (ppm): 193.36, 161.56, 145.51, 144.40, 143.42, 137.88, 133.50, 132.13, 123.65, 121.02, 120.94, 116.73, 116.26, 28.94, 20.88, 11.82. Anal. Calcd. For $C_{16}H_{15}N_3O_2$: C, 68.31; H, 5.37; N, 14.94. Found: C, 68.44; H, 5.49; N, 15.17.

4-(4-Acetyl-5-methyl-1H-pyrazol-1-yl)-6-methoxyquinolin-2(1H)-one (2c) Yellow powder, Yield: (95%); mp: 211–213 °C, ^{1}H NMR (400 MHz, DMSO-d_6) δ (ppm): 12.13 (s, 1H, NHCO), 8.39 (s, 1H), 7.40 (d, J = 9.0 Hz, 1H), 7.30 (d, J = 8.9 Hz, 1H), 6.74 (s, 1H), 6.41 (s, 1H), 3.65 (s, 3H, OCH_3), 2.49 (s, 3H, –CH_3), 2.44 (s, 3H, –CH_3). ^{13}C NMR (100 MHz, DMSO-d_6) δ (ppm): 193.74, 161.34, 155.01, 145.23, 144.53, 143.50, 134.31, 121.30, 121.11, 121.01, 117.82, 117.46, 106.21, 55.91, 29.28, 11.84. Anal. Calcd. For $C_{16}H_{15}N_3O_3$: C, 64.64; H, 5.09; N, 14.13. Found: C, 64.80; H, 5.21; N, 14.30.

4-(4Aacetyl-5-methyl-1H-pyrazol-1-yl)-6-chloroquinolin-2(1H)-one (2d) Dark yellow powder, Yield: (91%); mp: 229–231 °C, ^{1}H NMR (400 MHz, DMSO-d_6) δ (ppm): 12.34 (s, 1H, NHCO), 8.41 (s, 1H), 7.66 (dd, J = 8.8, 2.4 Hz, 1H), 7.45 (d, J = 8.8 Hz, 1H), 7.03 (d, J = 2.3 Hz, 1H), 6.86 (s, 1H), 2.49 (s, 3H, –CH_3), 2.47 (s, 3H, –CH_3). ^{13}C NMR (100 MHz, DMSO-d_6) δ (ppm): 193.38, 161.17, 144.55, 144.15, 143.43, 138.30, 131.83, 126.62, 123.35, 121.64, 120.82, 118.04, 117.64, 28.89, 11.66. Anal. Calcd. For $C_{15}H_{12}ClN_3O_2$: C, 59.71; H, 4.01; Cl, 11.75; N, 13.93; Found: C, 59.89; H, 4.23; N, 14.15.

4-(4-Acetyl-5-methyl-1H-pyrazol-1-yl)-6-bromoquinolin-2(1H)-one (2e) Brown powder, Yield: (86%); mp: 240–242 °C, ^{1}H NMR (400 MHz, DMSO-d_6) δ (ppm): 12.33 (s,

1H, NHCO), 8.41 (s, 1H), 7.76 (d, $J = 8.8$ Hz, 1H), 7.39 (d, $J = 8.8$ Hz, 1H), 7.16 (s, 1H), 6.84 (s, 1H), 2.49 (s, 3H), 2.47 (s, 3H). ^{13}C NMR (100 MHz, DMSO-d_6) δ (ppm): 193.53, 161.46, 144.85, 144.30, 143.74, 139.00, 134.74, 126.68, 121.94, 121.13, 118.52, 118.39, 114.24, 29.33, 12.11. Anal. Calcd. For $C_{15}H_{12}BrN_3O_2$: C, 52.04; H, 3.49. N, 12.14. Found: C, 52.16; H, 3.60; N, 12.37.

General synthetic procedure for (E)-4-(2-(1-(1-(6-substituted-2-oxo-1,2-dihydroquinolin-4-yl)-5-methyl-1H-pyrazol-4-yl) ethylidene)hydrazineyl)benzenesulfonamide derivatives. 4a–e and (E)-4-(2-(1-(1-(6-substituted-2-oxo-1,2-dihydroquinolin-4-yl)-5-methyl-1H-pyrazol-4-yl) ethylidene)hydrazineyl) benzoic acid derivatives. 4f–j

A sulfonamide phenylhydrazine derivative **3a** or carboxylic phenylhydrazine derivative **3b** (1.0 mmol) and 3 drops of glacial acetic acid were added to a suspension of compounds **2a–e** (1.0 mmol) in ethanol (20 mL). The reaction mixture was refluxed for 10–12 h. The precipitate that formed after cooling was filtered out, washed with diethyl ether, and crystallized from 20 mL of ethanol.

(E)-4-(2-(1-(5-methyl-1-(2-oxo-1,2-dihydroquinolin-4-yl)-1H-pyrazol-4-yl)ethylidene) hydrazineyl)benzenesulfonamide (4a) Pale yellow powder, yield: (76%); mp: 270–272 °C, ^{1}H NMR (400 MHz, DMSO-d_6) δ (ppm): 12.17 (s, 1H, NH), 9.59 (s, 1H), 8.09 (s, 1H), 7.68–7.53 (m, 3H), 7.44 (d, $J = 8.2$ Hz, 1H), 7.19 (m, 3H), 7.09–6.98 (m, 3H), 6.69 (s, 1H), 2.49 (s, 3H, –CH_3), 2.32 (s, 3H, –CH_3). ^{13}C NMR (100 MHz, DMSO-d_6) δ (ppm): 161.43, 148.78, 146.05, 140.24, 140.18, 139.32, 137.79, 133.04, 131.55, 127.25, 124.35, 122.37, 120.04, 116.74, 115.75, 111.57, 15.19, 12.59. HRMS (ESI, m/z) calcd for $[C_{21}H_{21}N_6O_3S]^+$ $(M+H)^+$ 437.1318, found. 437.1392.

(E)-4-(2-(1-(5-methyl-1-(6-methyl-2-oxo-1,2-dihydroquinolin-4-yl)-1H-pyrazol-4-yl) ethylidene)hydrazineyl)benzenesulfonamide (4b) White powder, yield: (87%); mp: 289–291 °C, ^{1}H NMR (400 MHz, DMSO-d_6) δ (ppm): 12.11 (s, 1H, NHCO), 9.59 (s, 1H), 8.10 (s, 1H), 7.64 (d, $J = 8.8$ Hz, 2H), 7.40 (dd, $J = 30.7$, 8.5 Hz, 2H), 7.22 (d, $J = 8.8$ Hz, 2H), 7.03 (s, 2H), 6.86 (s, 1H), 6.65 (s, 1H), 2.50 (s, 3H), 2.33 (s, 3H), 2.27 (s, 3H). ^{13}C NMR (100 MHz, DMSO-d_6) δ (ppm): 161.06, 148.79, 145.82, 140.24, 137.71, 137.43, 133.03, 132.86, 131.46, 127.25, 123.58, 120.02, 119.95, 116.69, 115.74, 111.57, 20.41, 15.18, 12.61. HRMS (ESI, m/z) calcd for $[C_{22}H_{23}N_6O_3S]^+$ $(M+H)^+$ 451.1474, found. 451.1551.

(E)-4-(2-(1-(1-(6-methoxy-2-oxo-1,2-dihydroquinolin-4-yl)-5-methyl-1H-pyrazol-4-yl) ethylidene)hydrazineyl) benzenesulfonamide (4c) White powder, yield: (77%); mp: 273–275 °C, ^{1}H NMR (400 MHz, DMSO-d_6) δ (ppm): 12.07 (s, 1H, NHCO), 9.58 (s, 1H), 8.10 (s, 1H), 7.63 (d, $J = 8.1$ Hz, 2H), 7.41–7.17 (m, 4H), 7.02 (s, 2H), 6.67 (s, 1H), 6.53 (s, 1H), 3.65 (s, 3H, –CH_3), 2.49 (d, $J = 5.0$ Hz, 3H, –CH_3), 2.31 (s, 3H –CH_3). ^{13}C NMR (100 MHz, DMSO-d_6) δ (ppm): 161.42, 154.86, 149.25, 145.92, 140.76, 140.67, 138.25, 134.42, 133.51, 127.73, 120.84, 120.53, 117.83, 117.68, 112.05, 106.67, 55.89, 15.66, 13.13. HRMS (ESI, m/z) calcd for $[C_{22}H_{231}N_6O_4S]^+$ $(M+H)^+$ 467.1423, found. 467.1497.

(E)-4-(2-(1-(1-(6-chloro-2-oxo-1,2-dihydroquinolin-4-yl)-5-methyl-1H-pyrazol-4-yl) ethylidene)hydrazineyl) benzenesulfonamide(4d) Pale yellow powder, yield: (74%); mp: 290–292 °C, ^{1}H NMR (400 MHz, DMSO-d_6) δ (ppm): 12.30 (s, 1H, NHCO), 9.60 (s, 1H), 8.13 (s, 1H), 7.65 (t, $J = 7.9$ Hz, 3H), 7.46 (d, $J = 8.8$ Hz, 1H), 7.22 (d, $J = 8.8$ Hz, 2H), 7.12 (s, 1H), 7.03 (s, 2H), 6.79 (s, 1H), 2.53 (s, 3H –CH_3), 2.32 (s, 3H –CH_3). ^{13}C NMR (100 MHz, DMSO-d_6) δ (ppm): 161.18, 148.75, 144.64, 140.60, 140.03, 138.22, 138.07, 133.08, 131.45, 127.25, 126.22, 123.57, 120.86, 120.29, 117.85, 117.80, 111.58, 15.20, 12.61. HRMS (ESI, m/z) calcd for $[C_{21}H_{20}ClN_6O_3S]^+$ $(M+H)^+$ 471.0928, found. 471.1002.

(E)-4-(2-(1-(1-(6-bromo-2-oxo-1,2-dihydroquinolin-4-yl)-5-methyl-1H-pyrazol-4-yl) ethylidene)hydrazineyl)benzenesulfonamide (4e) Pale yellow powder, yield: (78%); mp: 293–295 °C, ^{1}H NMR (400 MHz, DMSO-d_6) δ (ppm): 12.29 (s, 1H, NHCO), 9.61 (s, 1H), 8.14 (s, 1H), 7.76 (dd, $J = 8.8$, 2.1 Hz, 1H), 7.64 (d, $J = 8.8$ Hz, 2H), 7.39 (d, $J = 8.8$ Hz, 1H), 7.24 (dd, $J = 18.4$, 5.5 Hz, 3H), 7.03 (s, 2H), 6.78 (s, 1H), 2.53 (s, 3H), 2.32 (s, 3H). ^{13}C NMR (10 MHz, DMSO-d_6) δ (ppm): 161.41, 148.91, 144.82, 140.78, 140.22, 138.63, 138.26, 134.30, 133.15, 127.42, 126.69, 120.88, 120.46, 118.46, 118.22, 114.21, 111.76, 15.32, 12.76. HRMS (ESI, m/z) calcd for $[C_{21}H_{20}{}^{79}BrN_6O_3S]^+$ $(M+H)^+$ 515.0423, found. 515.0499.

(E)-4-(2-(1-(5-methyl-1-(2-oxo-1,2-dihydroquinolin-4-yl)-1H-pyrazol-4-yl)ethylidene) hydrazineyl)benzoic acid (4f) Pale yellow powder, yield: (81%); mp: 268–270 °C, ^{1}H NMR (400 MHz, DMSO-d_6) δ (ppm): 12.16 (s, 2H, COOH, NHCO), 9.58 (s, 1H), 8.07 (s, 1H), 7.77 (d, $J = 8.4$ Hz, 1H), 7.57 (t, $J = 7.4$ Hz, 1H), 7.42 (d, $J = 8.1$ Hz, 1H), 7.15 (d, $J = 8.3$ Hz, 1H), 7.04 (d, $J = 7.9$ Hz, 1H), 6.68 (s, 1H), 2.47 (s, 1H), 2.30 (s, 1H). ^{13}C NMR (100 MHz, DMSO-d_6) δ (ppm): 167.39, 161.47, 149.81, 146.09, 140.27, 140.20, 139.32, 137.80, 131.56, 131.02, 124.36, 122.39, 120.08, 120.04, 119.90, 116.75, 115.77, 111.59, 15.26, 12.59. HRMS (ESI, m/z) calcd for $[C_{22}H_{20}N_5O_3]^+$ $(M+H)^+$ 402.1488, found. 402.1557.

(E)-4-(2-(1-(5-methyl-1-(6-methyl-2-oxo-1,2-dihydroquinolin-4-yl)-1H-pyrazol-4-yl) ethylidene)hydrazineyl)benzoic acid (4g) Pale yellow powder, yield: (88%); mp: 255–257 °C, ^{1}H NMR (400 MHz, DMSO-d_6) δ (ppm): 12.20 (s, 1H, COOH), 12.10 (s, 1H, NHCO), 9.60 (s, 1H), 8.09 (s, 1H), 7.78 (d, J = 8.8 Hz, 2H), 7.42 (dd, J = 8.5, 1.7 Hz, 1H), 7.35 (d, J = 8.4 Hz, 1H), 7.17 (d, J = 8.8 Hz, 2H), 6.86 (s, 1H), 6.64 (s, 1H), 2.49 (s, 3H), 2.32 (s, 3H), 2.26 (s, 3H). ^{13}C NMR (100 MHz, DMSO-d_6) δ (ppm): 167.82, 161.74, 150.26, 146.29, 140.71, 140.69, 138.17, 137.89, 133.31, 131.92, 131.46, 124.05, 120.49, 120.43, 120.34, 117.15, 116.21, 112.04, 21.04, 15.72, 13.06. HRMS (ESI, m/z) calcd for $[C_{23}H_{22}N_5O_3]^+$ $(M+H)^+$ 416.1644, found. 416.1717.

(E)-4-(2-(1-(1-(6-methoxy-2-oxo-1,2-dihydroquinolin-4-yl)-5-methyl-1H-pyrazol-4-yl) ethylidene)hydrazineyl) benzoic acid (4h) Pale yellow powder, yield: (90%); mp: 288–290 °C, ^{1}H NMR (400 MHz, DMSO-d_6) δ (ppm): 12.08 (s, 2H, COOH), 12.08 (s, 2H, NHCO), 9.59 (s, 1H), 8.10 (s, 1H), 7.78 (d, J = 8.8 Hz, 2H), 7.39 (d, J = 9.0 Hz, 1H), 7.28 (dd, J = 9.0, 2.7 Hz, 1H), 7.17 (d, J = 8.8 Hz, 2H), 6.67 (s, 1H), 6.53 (d, J = 2.7 Hz, 1H), 3.65 (s, 3H), 2.56–2.43 (m, 6H), 2.32 (s, 3H). ^{13}C NMR (100 MHz, DMSO-d_6) δ (ppm): 167.83, 161.43, 154.86, 150.26, 145.93, 140.76, 140.66, 138.25, 134.42, 131.47, 120.85, 120.81, 120.56, 120.35, 117.83, 117.68, 112.05, 106.67, 55.88, 40.60, 40.39, 40.18, 39.97, 39.76, 39.55, 39.34, 15.64, 13.12. HRMS (ESI, m/z) calcd for $[C_{23}H_{22}N_5O_4]^+$ $(M+H)^+$ 431.1594, found. 416.1666.

(E)-4-(2-(1-(1-(6-chloro-2-oxo-1,2-dihydroquinolin-4-yl)-5-methyl-1H-pyrazol-4-yl) ethylidene)hydrazineyl) benzoic acid (4i) Pale yellow powder, yield: (78%); mp: 274–276 °C, ^{1}H NMR (400 MHz, DMSO-d_6) δ (ppm): 12.25 (s, 1H, COOH), 12.19 (s, 1H, s, 2H, COOH, NHCO), 9.58 (s, 1H), 8.09 (s, 1H), 7.75 (d, J = 7.8 Hz, 2H), 7.61 (d, J = 7.9 Hz, 1H), 7.42 (d, J = 8.5 Hz, 1H), 7.19–7.06 (m, 3H), 6.76 (s, 1H), 2.50 (s, 3H), 2.29 (s, 3H). ^{13}C NMR (100 MHz, DMSO-d_6) δ (ppm): 167.83, 161.66, 150.24, 145.12, 141.01, 140.50, 138.70, 138.53, 131.91, 131.47, 126.70, 124.06, 121.33, 120.78, 120.40, 118.32, 118.27, 112.06, 15.53, 13.09. HRMS (ESI, m/z) calcd for $[C_{22}H_{19}{}^{35}ClN_5O_3]^+$ $(M+H)^+$ 436.1098, found. 416.1192.

(E)-4-(2-(1-(1-(6-bromo-2-oxo-1,2-dihydroquinolin-4-yl)-5-methyl-1H-pyrazol-4-yl) ethylidene)hydrazineyl) benzoic acid (4j) Pale yellow powder, yield: (72%); mp: 281–283 °C, ^{1}H NMR (400 MHz, DMSO-d_6) δ (ppm): 12.29 (s, 2H, COOH), 12.29 (s, 2H, COOH, NHCO), 12.29 (s, 2H), 9.62 (s, 1H), 8.13 (s, 1H), 7.83–7.70 (m, 3H), 7.39 (d, J = 8.8 Hz, 1H), 7.27 (d, J = 2.1 Hz, 1H), 7.18 (d, J = 8.8 Hz, 2H), 6.78 (s, 1H), 2.54 (s, 3H), 2.33 (s, 3H). ^{13}C NMR (100 MHz, DMSO-d_6) δ (ppm): 167.83, 161.64, 150.23, 144.97, 141.09, 140.50, 139.01, 138.55, 134.56, 131.47, 127.04, 121.25, 120.78, 120.40, 118.77, 118.49, 114.42, 112.06, 15.65, 13.10. HRMS (ESI, m/z) calcd for $[C_{22}H_{19}{}^{79}BrN_3O_3]^+$ $(M+H)^+$ 480.0593, found. 480.0669.

Biology

Antiproliferative assay

Using Staurosporine as a control, the MTT assay was utilized to assess the antiproliferative effect of hybrids **4d**, **4e**, **4f**, and **4g** versus three human cancer cell lines: the leukemia (MOLT-4) cell line, the lung cancer (HOP-92) cell line, and the breast cancer (T47D) cell line. The median inhibitory concentration (IC_{50}) and GI_{50} (average IC_{50}) against the three cancer cell lines were calculated. See Appendix B.

EGFR inhibitory activity

The most potent Antiproliferative derivatives, **4d–g**, were tested for inhibitory effect against EGFR as a possible molecular target. Assessed using a 3-(4,5-dimethylthiazole-2-yl)-2,5-diphenyltetrazol (MTT) test. For more details, see Appendix B.

BRAFV600E inhibitory assay

Using Vemurafenib as the control medication, Compounds **4d**, **4e**, **4f**, and **4g** were further assessed for their inhibitory activity against $BRAF^{V600E}$. Refer to Appendix B for further information.

Docking study

Docking analyses of the most stable poses of 2-quinolone candidates incorporating pyrazole core **4d**, **4e**, **4f,** and **4g** along with the selected reference ligands: erlotinib and vemurafenib were accomplished against EGFR- and BRAF-active sites using Maestro software of Schrodinger 2022.4. The nominated biotargets are (1) EGFR (PDB ID: 1M17) [53] and (2) BRAF (PDB ID:5JRQ) [54] that were regained from RCSB protein data bank (PDB). The most stable conformers of the appointed 2-quinolones compounds and the biotargets reference ligands were built using ChemBiodraw 18.0 PerkinElmer software and cleaned up for bond alignment then imported with Schrodinger software in a 3D demonstration mode. The energy minimization has occurred using OPLS3e (Optimized Potentials for Liquid Simulations) [55] force field in Ligprep (Version 2022-4, Schrodinger) [56]. This minimization aids to assign bond orders, the hydrogens addition to the selected ligands, then the generated output files that denote the best poses of the ligands,

were further utilized for docking analyses. Furthermore, the indicated targets were displayed for preparation using Protein preparation wizard (Version 2022-4, Schrodinger) [56] as a main tool for protein preparation. The hydrogens have been added to the proteins, the charges, and the produced Het states using Epik at pH 7.0 ± 2.0 were allocated. The targets have been exposed to Pre-process, protein modification, and refinement by the applicable chain selection and the water molecules have been removed. Lastly, the targets have been minimized using OPLS3 force field. Besides, the receptor grids were constructed by considering the co-crystal ligands (X-ray pose of the ligand in the protein). The centroid of the ligands has been selected to establish a grid box around it and VanderWaal radius of the target atoms was scaled to 1.00 Å with a partial atomic charge of 0.25. The molecular docking has been run using performed glide rigid docking protocol [57] by means of Maestro software of Schrodinger. All the docking estimates have been done using Extra Precision (XP) mode, where a scaling factor of 0.8 and a partial atomic charge < 0.15 were employed to the atoms of proteins. Glide docking scoring has been devoted for verifying the best-docked poses from the output, and the interactions of these docked poses have been further investigated using XP visualizer. After the last step of docking with the co-crystal ligand in XP mode, root-mean-square deviation (RMSD) was ensured to authorize the target, and the RMSD values lie within the range of 0.46 Å.

Supplementary Information The online version contains supplementary material available at https://doi.org/10.1007/s11030-025-11127-4.

Author contribution Mohamed Ramadan, Tarek S. Ibrahim, Mohamed Alswah, and Ashraf H Bayoumi: supervision, conceptualization, editing, and revision. Mohamed M. Hawwas, Ahmed S. Mancy: methodology, formal analysis, writing, editing and docking study.

Funding Open access funding provided by The Science, Technology & Innovation Funding Authority (STDF) in cooperation with The Egyptian Knowledge Bank (EKB).

Data availability Data will be made available on request. The authors declare that the data supporting the findings of this study are available within the paper and its Supplementary Information files. Should any raw data files be needed in another format they are available from the corresponding author upon reasonable request.

Declarations

Conflict of interest The authors declare no conflict of interest.

Open Access This article is licensed under a Creative Commons Attribution 4.0 International License, which permits use, sharing, adaptation, distribution and reproduction in any medium or format, as long as you give appropriate credit to the original author(s) and the source, provide a link to the Creative Commons licence, and indicate if changes were made. The images or other third party material in this article are included in the article's Creative Commons licence, unless indicated otherwise in a credit line to the material. If material is not included in the article's Creative Commons licence and your intended use is not permitted by statutory regulation or exceeds the permitted use, you will need to obtain permission directly from the copyright holder. To view a copy of this licence, visit http://creativecommons.org/licenses/by/4.0/.

References

1. Sun M-Y, Bhaskar SM (2022) When two maladies meet: disease burden and pathophysiology of stroke in cancer. Int J Mol Sci 23(24):15769. https://doi.org/10.3390/ijms232415769
2. Ferlay J, Colombet M, Soerjomataram I, Parkin DM, Piñeros M, Znaor A, Bray F (2021) Cancer statistics for the year 2020: an overview. Int J Cancer 149(4):778–789. https://doi.org/10.1002/ijc.33588
3. Ahsan R, Khan MM, Mishra A, Noor G, Ahmad U (2023) Protein kinases and their inhibitors implications in modulating disease progression. J Protein Chem 42(6):621–632. https://doi.org/10.1007/s10930-023-10159-9
4. Zhang X, Thomas GM (2024) Recruitment, regulation and release: control of signaling enzyme localization and function by reversible S-acylation. J Biol Chem. https://doi.org/10.1016/j.jbc.2024.107696
5. Binamé F, Pham-Van LD, Bagnard D (2021) Manipulating oligodendrocyte intrinsic regeneration mechanism to promote remyelination. CMLS 78(13):5257–5273. https://doi.org/10.1007/s00018-021-03852-4
6. Patel S, Das A, Meshram P, Sharma A, Chowdhury A, Jariyal H, Datta A, Sarmah D, Nalla LV, Sahu B (2021) Pyruvate kinase M2 in chronic inflammations: a potpourri of crucial protein–protein interactions. Cell Biol Toxicol 37:653–678. https://doi.org/10.1007/s10565-021-09605-0
7. Li Q, Li Z, Luo T, Shi H (2022) Targeting the PI3K/AKT/mTOR and RAF/MEK/ERK pathways for cancer therapy. Mol Biomed 3(1):47. https://doi.org/10.1186/s43556-022-00110-2
8. Zhou S, Abdihamid O, Tan F, Zhou H, Liu H, Li Z, Xiao S, Li B (2024) KIT mutations and expression: current knowledge and new insights for overcoming IM resistance in GIST. JCCS 22(1):153. https://doi.org/10.1186/s12964-023-01411-x
9. Zhu C, Guan X, Zhang X, Luan X, Song Z, Cheng X, Zhang W, Qin J-J (2022) Targeting KRAS mutant cancers: from druggable therapy to drug resistance. Mol Cancer 21(1):159. https://doi.org/10.1186/s12943-022-01629-2
10. Zhou S, Abdihamid O, Tan F, Zhou H, Liu H, Li Z, Xiao S, Li B (2024) Resistance to anti-EGFR therapies in metastatic colorectal cancer: underlying mechanisms and reversal strategies. J Exp Clin Cancer Res 40:1–17. https://doi.org/10.1186/s13046-021-02130-2
11. Rodriquenz MG, Ciardiello D, Latiano TP, Maiorano BA, Martinelli E, Silvestris N, Ciardiello F, Maiello E (2022) Exploring biological heterogeneity and implications on novel treatment paradigm in BRAF-mutant metastatic colorectal cancer. Crit Rev Oncol Hematol 173:103657. https://doi.org/10.1016/j.critrevonc.2022.103657
12. Al Bostami RD, Abuwatfa WH, Husseini GA (2022) Recent advances in nanoparticle-based co-delivery systems for cancer therapy. J Nanomater 12(15):2672. https://doi.org/10.3390/nano12152672
13. Berretta M, Dal Lago L, Tinazzi M, Ronchi A, La Rocca G, Montella L, Di Francia R, Facchini BA, Bignucolo A, Montopoli M (2022) Evaluation of concomitant use of anticancer drugs and herbal products: from interactions to synergic activity. Cancers 14(21):5203. https://doi.org/10.3390/cancers14215203
14. Gilad Y, Gellerman G, Lonard DM, O'malley BW (2021) Drug combination in cancer treatment—From cocktails to conjugated

combinations. Cancers 13(4):669. https://doi.org/10.3390/cancers13040669
15. Shi K, Wang G, Pei J, Zhang J, Wang J, Ouyang L, Wang Y, Li W (2022) Emerging strategies to overcome resistance to third-generation EGFR inhibitors. J Hematol Oncol 15(1):94. https://doi.org/10.1186/s13045-022-01311-6
16. Ge M, Zhu Y, Wei M, Piao H, He M (2023) Improving the efficacy of anti-EGFR drugs in GBM: where we are going? Biochim Biophys Acta Rev Cancer. https://doi.org/10.1016/j.bbcan.2023.188996
17. Yang J-J, Fang J, Shu Y-Q, Chang J-H, Chen G-Y, He JX, Li W, Liu X-Q, Yang N, Zhou C (2021) A phase Ib study of the highly selective MET-TKI savolitinib plus gefitinib in patients with EGFR-mutated, MET-amplified advanced non-small-cell lung cancer. Invest New Drugs 39:477–487. https://doi.org/10.1007/s10637-020-01010-4
18. Nitulescu GM, Stancov G, Seremet OC, Nitulescu G, Mihai DP, Duta-Bratu CG, Barbuceanu SF, Olaru OT (2023) The importance of the pyrazole scaffold in the design of protein kinases inhibitors as targeted anticancer therapies. Molecules 28(14):5359. https://doi.org/10.3390/molecules28145359
19. El-Damasy AK, Salem MS, Sebaiy MM, Elgawish MS (2024) p38 mitogen-activated protein kinase inhibitors. In: Current molecular targets of heterocyclic compounds for cancer therapy. Elsevier, Amsterdam, pp 219–254. https://doi.org/10.1016/B978-0-323-96121-9.00011-5
20. Sieber J, Wieder N, Clark A, Reitberger M, Matan S, Schoenfelder J, Zhang J, Mandinova A, Bittker JA, Gutierrez J (2018) GDC-0879, a $BRAF^{V600E}$ inhibitor, protects kidney podocytes from death. Cell Chem Biol 25(2):175–184. https://doi.org/10.1016/j.chembiol.2017.11.006
21. Shiri P, Ramezanpour S, Amani AM, Dehaen W (2022) A patent review on efficient strategies for the total synthesis of pazopanib, regorafenib and lenvatinib as novel anti-angiogenesis receptor tyrosine kinase inhibitors for cancer therapy. Mol Divers 26(5):2981–3002. https://doi.org/10.1007/s11030-022-10406-8
22. Goldman JW, Bueno AM, Dooms C, Jhaveri K, de Miguel M, Piha-Paul SA, Unni N, Zick A, Mahipal A, Suga JM (2024) Neratinib efficacy in patients with EGFR Exon 18-mutant non-small-cell lung cancer: findings from the SUMMIT basket trial: Neratinib for EGFR Exon 18-mutant NSCLC. Clin Lung Cancer 23:121. https://doi.org/10.1016/j.cllc.2024.12.003
23. Gaber AA, Sharaky M, Elmaaty AA, Hammouda MM, Mourad AA, Elkhawaga SY, Mokhtar MM, Abouzied AS, Mourad MA, Al-Karmalawy AA (2023) Design and synthesis of novel pyrazolopyrimidine candidates as promising EGFR-T790M inhibitors and apoptosis inducers. Future Med Chem 15(19):1773–1790. https://doi.org/10.4155/fmc-2023-0156
24. Maji L, Teli G, Raghavendra NM, Sengupta S, Pal R, Ghara A, Matada GSP (2024) An updated literature on BRAF inhibitors (2018–2023). Mol Divers 28(4):2689–2730. https://doi.org/10.1007/s11030-023-10699-3
25. Mohassab AM, Hassan HA, Abdelhamid D, Gouda AM, Youssif BG, Tateishi H, Fujita M, Otsuka M, Abdel-Aziz M (2021) Design and synthesis of novel quinoline/chalcone/1,2,4-triazole hybrids as potent antiproliferative agent targeting EGFR and $BRAF^{V600E}$ kinases. Bioorg Chem 106:104510. https://doi.org/10.1016/j.bioorg.2020.104510
26. Al-Wahaibi LH, Youssif BG, Abou-Zied HA, Bräse S, Brown AB, Tawfeek HN, El-Sheref EM (2024) Synthesis of a new series of 4-pyrazolylquinolinones with apoptotic antiproliferative effects as dual EGFR/$BRAF^{V600E}$ inhibitors. RSC Med Chem 15(7):2538–2552. https://doi.org/10.1039/D4MD00230J
27. Lamie PF, El-Kalaawy AM, Latif NSA, Rashed LA, Philoppes JN (2021) Pyrazolo [3,4-d] pyrimidine-based dual EGFR T790M/HER2 inhibitors: design, synthesis, structure–activity relationship and biological activity as potential antitumor and anticonvulsant agents. Eur J Med Chem 214:113222. https://doi.org/10.1016/j.ejmech.2021.113222
28. Pal R, Teli G, Sengupta S, Maji L, Purawarga Matada GS (2024) An outlook of docking analysis and structure-activity relationship of pyrimidine-based analogues as EGFR inhibitors against non-small cell lung cancer (NSCLC). J Biomol Struct Dyn 42(18):9795–9811. https://doi.org/10.1080/07391102.2023.2252082
29. Srisongkram T, Tookkane D (2024) Insights into the structure-activity relationship of pyrimidine-sulfonamide analogues for targeting $BRAF^{V600E}$ protein. Biophys Chem 307:107179. https://doi.org/10.1016/j.bpc.2024.107179
30. Bouabdallah S (2024) Enzyme inhibitors: design of kinase inhibitors as anticancer drugs. In: Biochemical and molecular pharmacology in drug discovery. Elsevier, Amsterdam, pp 283–296. https://doi.org/10.1016/B978-0-443-16013-4.00013-0
31. Fawzy MA, Ibrahim KH, Aly AA, Mohamed AH, Naguib Abdel Hafez SM, Abdelzaher WY, Elkaeed EB, Alsfouk AA, Abdelhafez E-SM (2024) One-pot synthesis and pharmacological evaluation of new quinoline/pyrimido-diazepines as pulmonary antifibrotic agents. Future Med Chem 2024:1–20. https://doi.org/10.1080/17568919.2024.2394018
32. Vahedpour T, Hamzeh-Mivehroud M, Hemmati S, Dastmalchi S (2021) Synthesis of 2-pyrazolines from hydrazines: mechanisms explained. ChemistrySelect 6(25):6483–6506. https://doi.org/10.1002/slct.202101467
33. Haji N, Faizi M, Koutentis PA, Carty MP, Aldabbagh F (2023) Heterocyclic iminoquinones and quinones from the National Cancer Institute (NCI, USA) COMPARE analysis. Molecules 28(13):5202. https://doi.org/10.3390/molecules28135202
34. Zaraei S-O, Al-Ach NN, Anbar HS, El-Gamal R, Tarazi H, Tokatly RT, Kalla RR, Munther MA, Wahba MM, Alshihabi AM (2022) Design and synthesis of new quinoline derivatives as selective C-RAF kinase inhibitors with potent anticancer activity. Eur J Med Chem 238:114434. https://doi.org/10.1016/j.ejmech.2022.114434
35. Ghasemi M, Liang S, Luu QM, Kempson I (2023) The MTT assay: a method for error minimization and interpretation in measuring cytotoxicity and estimating cell viability. In: Cell viability assays: methods and protocols. Springer, New York, pp 15–33. https://doi.org/10.1007/978-1-0716-3052-5_2
36. Khirallah SM, Ramadan HM, El-Deen IM, El Rayess RA (2023) Design, synthesis, and antiproliferative activities of 1, 3-disubstituted 2-thioxoimidazolidin-4-one derivatives against HepG2 and MCF-7 cells. ChemistrySelect 8(32):1098. https://doi.org/10.1002/slct.202301098
37. Zaki I, Imam AM (2020) Design, synthesis, and cytotoxic screening of new quinoline derivatives over MCF-7 breast cancer cell line. Russ J Appl Chem 6:1099–1109. https://doi.org/10.1134/S1068162020060096
38. Shi K, Wang G, Pei J, Zhang J, Wang J, Ouyang L, Li W (2022) Emerging strategies to overcome resistance to third-generation EGFR inhibitors. J Hematol Oncol 15(1):94. https://doi.org/10.1186/s13045-022-01311-6
39. Roskoski R Jr (2020) Properties of FDA-approved small molecule protein kinase inhibitors: a 2020 update. Pharmacol Res 152:104609. https://doi.org/10.1016/j.phrs.2019.104609
40. Vulpetti A, Bosotti R (2004) Sequence and structural analysis of kinase ATP pocket residues. Farmaco 59(10):759–765. https://doi.org/10.1016/j.farmac.2004.05.010
41. Hu X, Wang D, Tong Y, Tong L, Wang X, Zhu L, Xie H, Li S, Yang Y, Xu Y (2017) Design, synthesis, and evaluation of ribose-modified anilinopyrimidine derivatives as EGFR tyrosine kinase inhibitors. Fchem 5:01. https://doi.org/10.3389/fchem.2017.00101

42. Tsou H-R, Mamuya N, Johnson BD, Reich MF, Gruber BC, Ye F, Nilakantan R, Shen R, Discafani C, DeBlanc R (2001) 6-Substituted-4-(3-bromophenylamino) quinazolines as putative irreversible inhibitors of the epidermal growth factor receptor (EGFR) and human epidermal growth factor receptor (HER-2) tyrosine kinases with enhanced antitumor activity. J Med Chem 44(17):2719–2734. https://doi.org/10.1021/jm0005555
43. Trumpp-Kallmeyer S, Rubin JR, Humblet C, Hamby JM, Hollis Showalter H (1998) Development of a binding model to protein tyrosine kinases for substituted pyrido [2,3-d] pyrimidine inhibitors. J Med Chem 41(11):1752–1763. https://doi.org/10.1021/jm970634p
44. García-Echeverría C, Traxler P, Evans DB (2000) ATP site-directed competitive and irreversible inhibitors of protein kinases. Med Res Rev 20(1):28–57. https://doi.org/10.1002/(sici)1098-1128(200001)20:1%3c28::aid-med2%3e3.0.co;2-2. (**PMID: 10608920**)
45. Heinrich T, Seenisamy J, Emmanuvel L, Kulkarni SS, Bomke J, Rohdich F, Greiner H, Esdar C, Krier M, Grädler U (2013) Fragment-based discovery of new highly substituted 1 H-pyrrolo [2,3-b]-and 3 H-imidazolo [4,5-b]-pyridines as focal adhesion kinase inhibitors. J Med Chem 56(3):1160–1170. https://doi.org/10.1021/jm3016014
46. Stamos J, Sliwkowski MX, Eigenbrot C (2002) Structure of the epidermal growth factor receptor kinase domain alone and in complex with a 4-anilinoquinazoline inhibitor. JBC 277(48):46265–46272. https://doi.org/10.1074/jbc.M207135200
47. Colombino M, Casula M, Paliogiannis P, Manca A, Sini MC, Pisano M, Santeufemia DA, Cossu A, Palmieri G (2024) Heterogeneous pathogenesis of melanoma: BRAF mutations and beyond. Crit Rev Oncol Hematol 11:104435. https://doi.org/10.1016/j.critrevonc.2024.104435
48. Lu X (2023) 2-Aminopyrimidine: a privileged scaffold in kinase drug discovery. In: Privileged scaffolds in drug discovery. Elsevier, Amsterdam, pp 391–404. https://doi.org/10.1016/B978-0-443-18611-0.00012-7
49. Sanchez JN, Wang T, Cohen MS (2018) BRAF and MEK inhibitors: use and resistance in BRAF-mutated cancers. Drugs 78(5):549–566. https://doi.org/10.1007/s40265-018-0884-8
50. Grasso M, Estrada MA, Ventocilla C, Samanta M, Maksimoska J, Villanueva J, Winkler JD, Marmorstein R (2016) Chemically linked vemurafenib inhibitors promote an inactive $BRAF^{V600E}$ conformation. ACS Chem Biol 11(10):2876–2888. https://doi.org/10.1021/acschembio.6b00529
51. Hegazy ME, Taher ES, Ghiaty AH, Bayoumi AH (2024) Tailored quinoline hybrids as promising COX-2/15-LOX dual inhibitors endowed with diverse safety profile: Design, synthesis, SAR, and histopathological study. Bioorg Chem 145:107244. https://doi.org/10.1016/j.bioorg.2024.107244
52. Haque MA, Marathakam A, Rana R, Almehmadi SJ, Tambe VB, Charde MS, Islam F, Siddiqui FA, Culletta G, Almerico AM, Tutone M (2023) Fighting antibiotic resistance: new Pyrimidine-Clubbed Benzimidazole derivatives as potential DHFR inhibitors. Molecules 28(2):501. https://doi.org/10.3390/molecules28020501
53. Altıntop MD, Ertorun İ, Çiftçi GA, Özdemir A (2024) Design, synthesis and biological evaluation of a new series of imidazothiazole-hydrazone hybrids as dual EGFR and Akt inhibitors for NSCLC therapy. Eur J Med Chem 276:116698. https://doi.org/10.1016/j.ejmech.2024.116698
54. El-Kalyoubi SA, Gomaa HA, Abdelhafez EM, Ramadan M, Agili F, Youssif BG (2023) Design, synthesis, and anti-proliferative action of purine/pteridine-based derivatives as dual inhibitors of EGFR and $BRAF^{V600E}$. J Pharm 16(5):716. https://doi.org/10.3390/ph16050716
55. Pugazhendhi S, Murugesan T, Dhanapal AR, Balakrishnan A, Venkidasamy B, Vedagiri H, Arvind Prasanth D (2023) Inhibition of mecA and blaCTX-M from MRSA and ESBL strains of diabetic foot infection by screening antibiotics compound library: an in silico analysis. J Biomol Struct Dyn 41(21):11431–11436. https://doi.org/10.1080/07391102.2022.2162581
56. Lanka G, Bathula R, Ghosh B, Potlapally SR (2023) Identification of potential antiviral lead inhibitors against SARS-CoV-2 Main protease: structure-guided virtual screening, docking, ADME, and MD simulation based approach. Artif Intell Chem 1(2):100015. https://doi.org/10.1016/j.aichem.2023.100015
57. Kumar BH, Manandhar S, Mehta CH, Nayak UY, Pai KSR (2022) Structure-based docking, pharmacokinetic evaluation, and molecular dynamics-guided evaluation of traditional formulation against SARS-CoV-2 spike protein receptor bind domain and ACE2 receptor complex. Chem Pap 76:1063–1083. https://doi.org/10.1007/s11696-021-01917-z

Publisher's Note Springer Nature remains neutral with regard to jurisdictional claims in published maps and institutional affiliations.